Publications of the Astronomical Society of the Pacific, 132:035003 (29pp), 2020 March https://doi.org/10.1088/1538-3873/ab67ec

In-flight Performance and Calibration of the LOng Range Reconnaissance Imager (LORRI) for the *New Horizons* Mission

H. A. Weaver[1], A. F. Cheng[1], F. Morgan[1], H. W. Taylor[1], S. J. Conard[1], J. I. Nunez[1], D. J. Rodgers[1], T. R. Lauer[2], W. M. Owen[3], J. R. Spencer[4], O. Barnouin[1], A. S. Rivkin[1], C. B. Olkin[4], S. A. Stern[4], L. A. Young[4], M. B. Tapley[5], and M. Vincent[4]

[1] Johns Hopkins University Applied Physics Laboratory, 11100 Johns Hopkins Road, Laurel, MD 20723-6099, USA; hal.weaver@jhuapl.edu
[2] NSF's National Optical-Infrared Astronomy Research Laboratory, P.O. Box 26732, Tucson, AZ 85726, USA
[3] Jet Propulsion Laboratory, 4800 Oak Grove Drive, Pasadena, CA 91109, USA
[4] Southwest Research Institute, 1050 Walnut Street, Suite 300, Boulder, CO 80302, USA
[5] Southwest Research Institute, 6220 Culebra Road, San Antonio, TX 78238, USA
Received 2019 November 11; accepted 2020 January 2; published 2020 February 18

Abstract

The LOng Range Reconnaissance Imager (LORRI) is a panchromatic (360–910 nm for the wavelengths where the responsivity falls to 10% of the peak value), narrow-angle (field of view = 0.°29), high spatial resolution (pixel scale = 1.″02) visible light imager used on NASA's *New Horizons* (*NH*) mission for both science observations and optical navigation. Calibration observations began several months after the *New Horizons* launch on 2006 January 19 and have been repeated approximately annually throughout the course of the mission, which is ongoing. This paper describes the in-flight LORRI calibration measurements, and the results derived from our analysis of the calibration data. LORRI has been remarkably stable over time with no detectable changes (at the ∼1% level) in sensitivity or optical performance since launch. The point-spread function varies over the FOV but is well-characterized and stable, enabling accurate deconvolution to recover the highest possible spatial resolution during observations of resolved targets, especially when multiple, overlapping images are obtained. By employing 4 × 4 re-binning of the CCD pixels during read out, a special spacecraft tracking mode, exposure times of ∼30 s, and co-addition of ∼100 images, LORRI can detect unresolved targets down to $V \approx 22$ with a signal-to-noise ratio (S/N) of ∼5. LORRI images have an instantaneous dynamic range of ∼3500, which combined with exposure time control ranging from 0 ms to 64,967 ms in 1 ms steps supports high resolution, high sensitivity imaging of planetary targets spanning heliocentric distances from Jupiter to deep in the Kuiper Belt, enabling a wide variety of scientific investigations. We describe here how to transform LORRI images from raw (engineering) units into scientific (calibrated) units for both resolved and unresolved targets. Assuming that the wavelength variation of LORRI's sensitivity is accurately described by the ground-based calibration, we estimate that LORRI's absolute sensitivity is accurate to ∼2% (1σ) for targets with solar-type spectral energy distributions (SEDs). The accuracy of the absolute calibration for targets with other SEDs should be comparably good when employing synthetic photometry techniques, which we do when deriving LORRI's photometry keywords. We also describe various instrumental artifacts that could affect the interpretation of LORRI images under some observing circumstances.

Key words: instrumentation: detectors – space vehicles: instruments – techniques: image processing – techniques: photometric

Online material: color figures

1. Introduction to the LOng Range Reconnaissance Imager (LORRI)

The LORRI is a narrow angle (FOV = 0.°291), high spatial resolution (IFOV = 1.″02), Ritchey–Chrétien telescope with a 20.8 cm diameter primary mirror, a focal length of 262 cm, and a three lens field-flattening assembly (Figure 1).

The telescope, its lens assembly, and its baffle together are referred to as the Optical Telescope Assembly (OTA), which was provided by SSG Precision Optronics, now L3 Harris SSG. The telescope metering structure and its two mirrors are constructed from silicon carbide, providing an optical design that maintains focus from +50 °C to −120 °C without the use of a focus mechanism when mounted within the *New Horizons* spacecraft. LORRI's only moving part is a once-open aperture cover mounted to the *New Horizons* spacecraft, which was opened on 2006 August 29, after LORRI was allowed to outgas for decontamination purposes at a temperature of approximately +50 °C for approximately 7 months. After the door

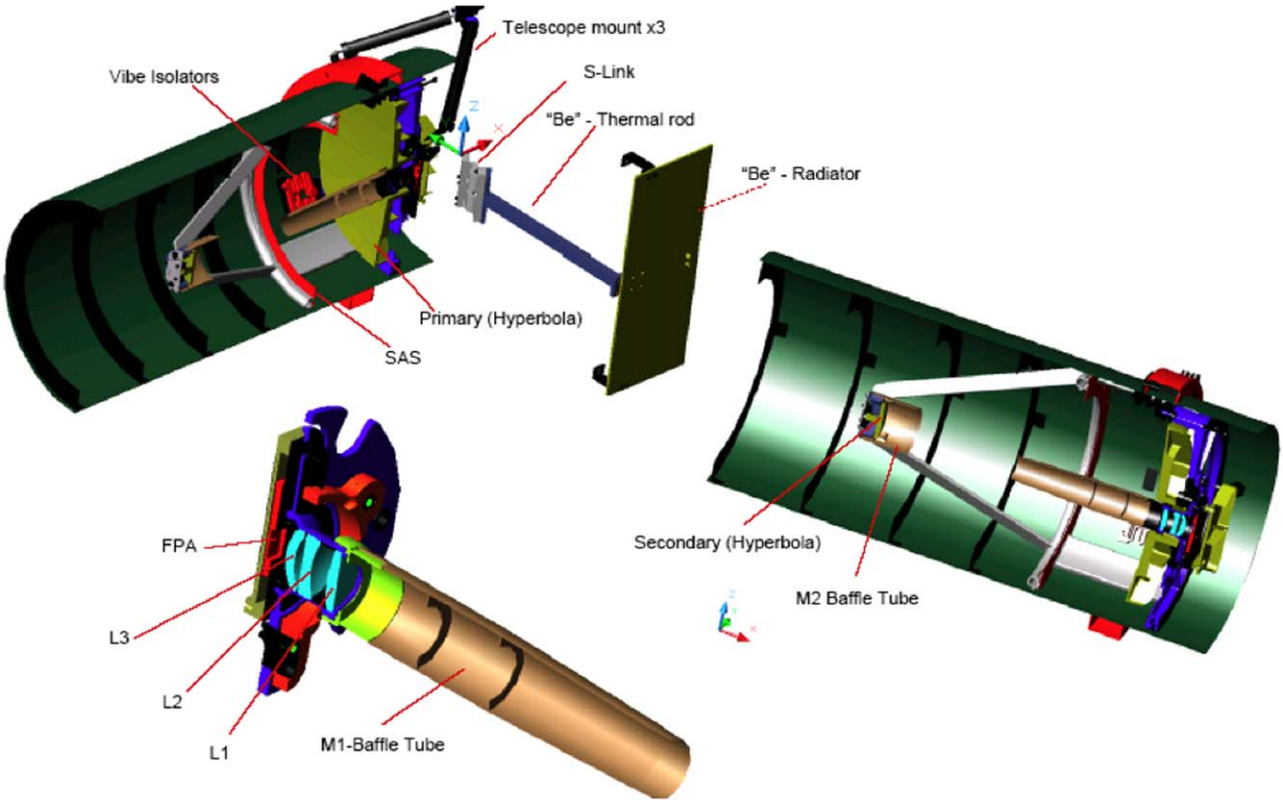

Figure 1. Computer Aided Design (CAD) views of LORRI. "M1" refers to the primary mirror, "M2" refers to the secondary mirror, "FPA" refers to the focal plane assembly, "Be" refers to beryllium components, and "SAS" refers to the system aperture stop. "L1," "L2," and "L3" refer to the 3 separate lenses of the field-flattening lens assembly.
(A color version of this figure is available in the online journal.)

opened, the OTA mirrors have generally remained within several degrees of −70 °C, except when a heater is turned on to promote additional decontamination, when the OTA mirror temperatures rise to approximately −35 °C. Table 1 details how many times the 10 W decontamination heater has been activated during the course of the mission.

Figure 2 shows the LORRI OTA during laboratory testing, LORRI's location within the *New Horizons* spacecraft, and the locations of all the instruments on the *New Horizons* spacecraft. The boresights of the three remote sensing instruments (LORRI, Ralph, and Alice) are approximately co-aligned.

A 1024 × 1024 pixel (optically active region), back-thinned, backside-illuminated CCD detector (model CCD 47–20 from e2v, now Teledyne-e2v) is located at the telescope focal plane and is operated in standard frame-transfer mode. The LORRI CCD incorporates anti-blooming technology to eliminate bleeding of the electrons along columns when bright targets saturate (i.e., when the signal in a pixel exceeds the full-well capacity of ∼80,000 electrons). The optically active area of the CCD has a "midband" anti-reflection coating that provides high quantum efficiency across the visible portion of the spectrum, exceeding ∼90% at wavelengths near the peak efficiency (see further discussion later). For the highest resolution observations, all optically active pixels are read out from the CCD ("1 × 1" format). But the pixels can be also be re-binned by a factor of 4 in each direction (i.e., column and row directions) during CCD readout ("4 × 4" format), which reduces the data volume by a factor of 16 and results in an effective pixel size of IFOV = 4.″08. During readout in either format, the analog signals are processed using correlated double-sampling and converted to data numbers (DNs) using a 12 bit analog-to-digital converter, yielding a valid DN integer range from 0 to 4095.

In addition to the optically active pixels, four columns (one column in 4 × 4 format) in the non-illuminated region of the CCD are read out to provide a measurement of the bias level and dark current for each image. The bias level is ∼540 DN but varies linearly with the temperature of the focal plane electronics (FPE) board. The readout of the extra CCD columns enables accurate tracking of the bias level for each image. Further discussion of how the calibration pipeline determines the bias level is provided below.

The electronics noise, which includes the CCD read noise, is ∼1.1 DN. The electronics noise is monitored throughout the mission by differencing two bias images (i.e., with commanded exposure times of 0 ms), which are obtained during each annual

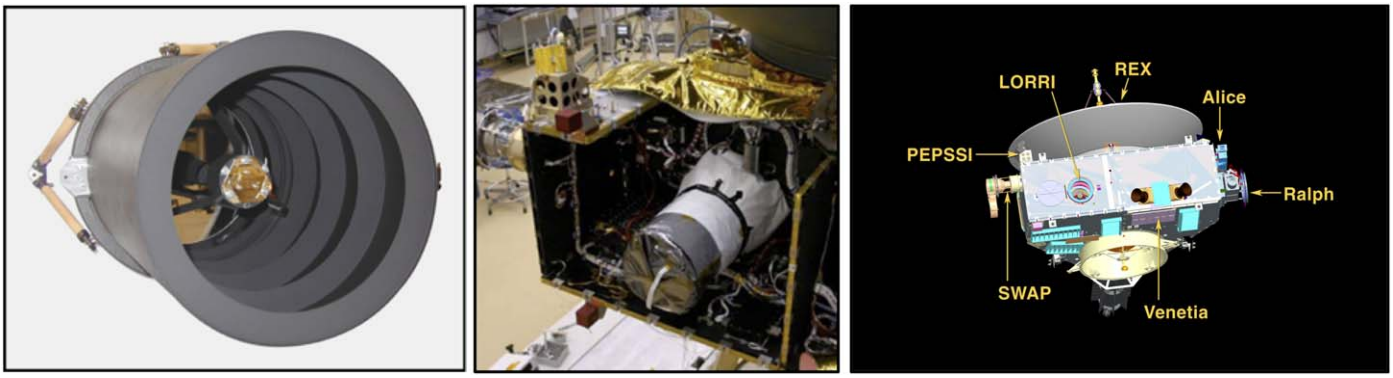

Figure 2. The image on the left shows a completely assembled LORRI on a lab bench during ground testing. The middle image shows where LORRI is mounted within the *New Horizons* spacecraft. The image on the right is a drawing showing the locations of all the instruments on the *New Horizons* spacecraft. The diameter of the high gain antenna, which feeds the REX instrument, is 2.1 m. Short descriptions of all the *New Horizons* instruments can be found in Weaver et al. (2008). Reproduced from Exo-Transit. Reprinted with permission from AAAS.
(A color version of this figure is available in the online journal.)

Table 1
LORRI Decontamination Activities

Year	Number of Decontamination Activities
2006	2[a]
2007	8
2008	6
2009	2
2010	3
2011	3
2012	2
2013	2
2014	3
2015	3
2016	3
2017	4
2018	1
2019	1

Notes. A "decontamination activity" involves turning on the 10 W decontamination heater for at least 24 hr, and sometimes for as long as ∼6 months. In 2018–2019, we showed that the 10 W decontamination heater can be turned off for at least 6 months without affecting LORRI's optical performance. Thus, we plan to have fewer decontamination activities during post-2019 operations, typically once per year.
[a] After the LORRI front aperture door was opened on 2006 August 29, there were two additional decontamination activities that year. From launch on 2006 January 19 until the door was opened, LORRI was allowed to outgas for decontamination purposes at a temperature of approximately +50 °C.

checkout. Following the technique outlined by Janesick (2001), we randomly sample 25 × 25 pixel subarrays (7 × 7 pixel subarrays for 4 × 4 images) of the difference image for 50,000 randomly selected regions across the entire CCD to obtain a histogram of noise values. Examples of noise histograms obtained both early in the mission (2009 July) and more recently (2019 July) are shown in Figure 3. Since the histograms are not completely symmetrical (the images have cosmic rays), neither the average value nor the median value give the best representation of the noise. Rather, we use an eyeball estimate of the peak in the histogram, after generating the histogram multiple times (since random numbers are used to determine the box centers, the computer program produces a slightly different histogram each time it is run), as our best estimate of the actual electronics noise. The effective dynamic range for a single image is ∼3500, which is the largest DN value available (after accounting for the bias level) divided by the noise.

The electronics gain, which is the scale factor that enables conversion from electrons detected to DN, is slightly different for 1 × 1 versus 4 × 4 images. Again, we follow the technique outlined by Janesick (2001) to produce a gain histogram for each of the two CCD formats using two well-exposed images with essentially constant illumination over the entire CCD. In this case, however, we use differences of two flat field images taken from the post-environmental calibration conducted in 2004 September, prior to launch, to produce gain histograms because no in-flight flat fields could be obtained. Examples of gain histograms are shown in Figure 4, and they clearly show that 4 × 4 images have a slightly higher gain than 1 × 1 images. This same behavior has been seen in flight when observing the same targets in the two different CCD formats. For example, in 2008 October when taking alternating 1 × 1 and 4 × 4 images of solar stray light while the spacecraft rolled about the LORRI boresight at a fixed solar elongation angle of ∼13°, the ratios of the median signal rates was ∼17.3 (4 × 4/1 × 1) rather than the expected value of 16. Similarly, the integrated signals of stars (in DN s^{-1}) appear to be ∼8% larger in 4 × 4 images compared to 1 × 1 images of the same fields. We have adopted gain values of 21.0 e DN^{-1} and 19.4 e DN^{-1} for 1 × 1 and 4 × 4 images, respectively, which are consistent

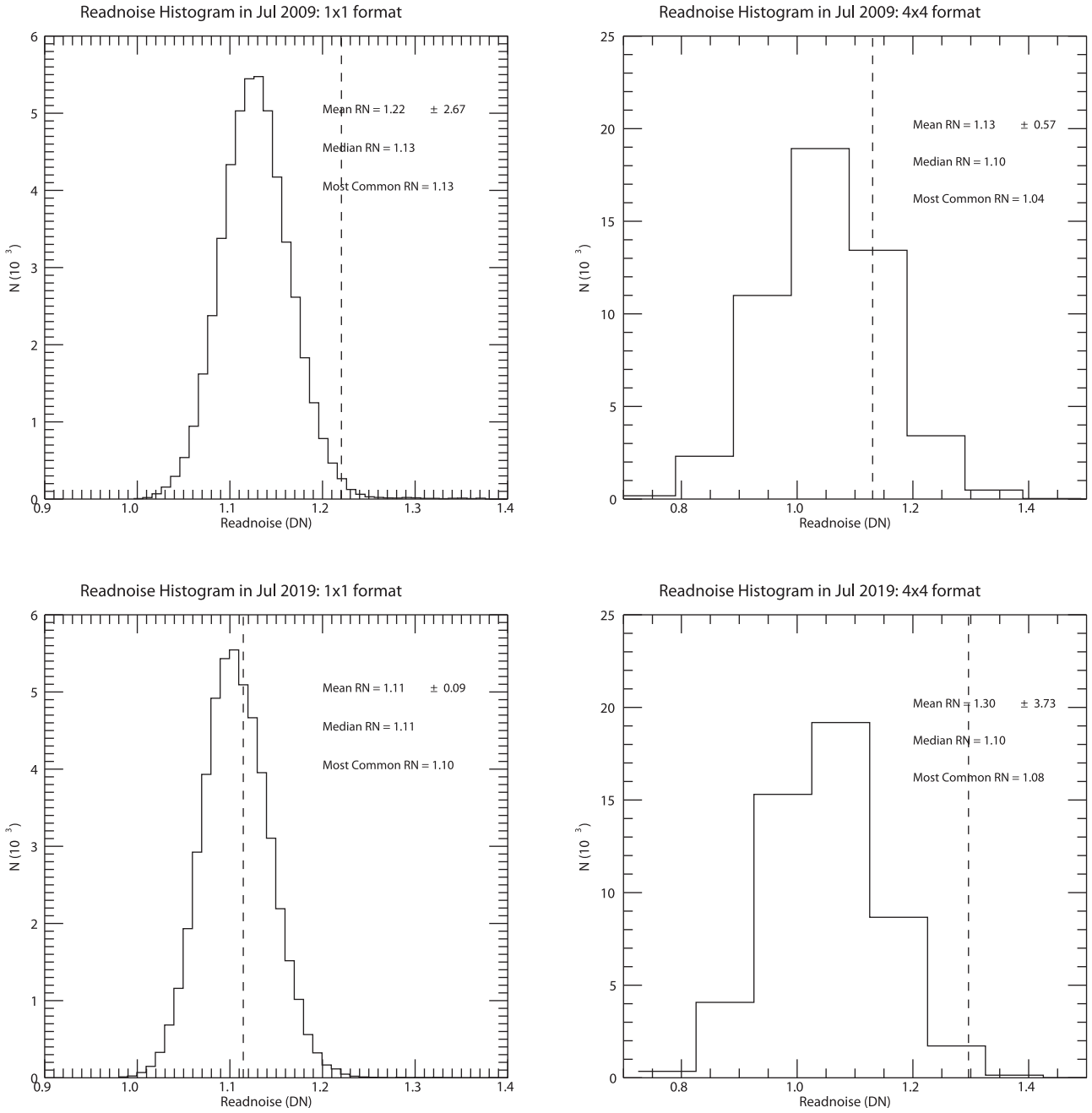

Figure 3. These figures show in-flight electronics noise histograms for LORRI at two different epochs separated by 10 yr: 2009 July data are shown along the top row and 2019 July data are shown along the bottom row. The figures on the left are for 1 × 1 CCD format, and the figures on the right are for 4 × 4 CCD format. The mean (dashed vertical line), standard deviation, and median values are displayed for each histogram, but the most common values (also displayed) should be more representative of the true electronics noise. In any case, there has been essentially no change in the electronics noise over the entire *New Horizons* mission.

with both the pre-launch and post-launch data. With these gain values, the full well capacity of the CCD is nicely matched to the full range of the analog-to-digital converter.

LORRI's response is linear to within 1% over its entire dynamic range, as demonstrated during both ground testing (Morgan et al. 2005) and in-flight observations taken over a range of different exposure times. Cooling of the CCD is provided by a beryllium radiator, which is painted white and is connected to the back end of the CCD mount via an S-link and a conduction rod. The radiator is exposed to space on the side of the spacecraft opposite that of the high gain antenna. During a period of outgassing with the aperture door closed during the first 7 months of the *New*

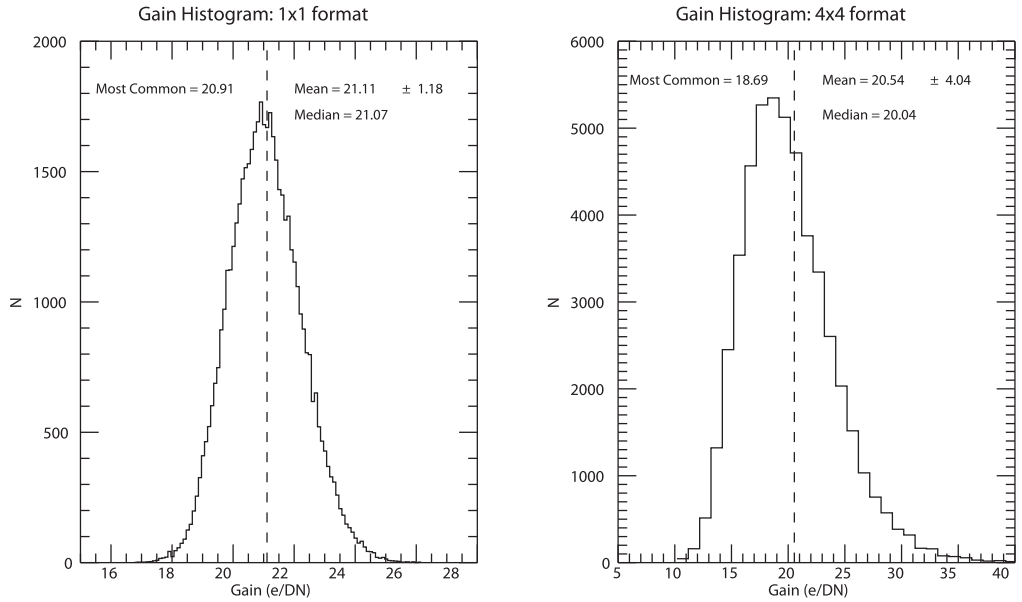

Figure 4. These figures show gain histograms obtained during ground testing for each of the two CCD formats. For both 1 × 1 format (left) and 4 × 4 format (right), the means (dashed vertical lines), standard deviations, and median values are displayed for the histograms, but the most common values (also displayed) should be more representative of the true electronics gain. As discussed in the text, we have adopted a gain of 21.0 e DN^{-1} for 1 × 1 format and 19.4 e DN^{-1} for 4 × 4 format.

Horizons mission, the CCD temperature was warmed to ∼30 °C. Periodically throughout the mission (see Table 1), a 10 W decontamination heater is used to warm the CCD to approximately −35 °C to prevent accumulation of any outgassed contaminants. Otherwise, the LORRI CCD temperature has been stable at approximately −80 °C throughout the mission, which is low enough that dark current is negligible for all 1 × 1 format images. Dark current is detectable in "warm" pixels during long exposures taken in 4 × 4 format. The location and number of warm pixels is variable, but is always <1% of the total number of pixels.

As is the case for all imagers using CCDs, the charge transfer efficiency (CTE) is less than 100%, which can result in lower signal rates for targets located at high row numbers (i.e., farthest from the serial transfer output) and potential degradation of the PSF. We did not independently measure the CTE, but the manufacturer's specification sheet gives CTE values of 0.999993 for serial direction transfers (i.e., along the row direction) and 0.999999 for parallel direction transfers (i.e., along the column direction). Measurements of stars in different regions of the CCD (described later) suggest no change in the CCD CTE values over the course of the mission at the level of ∼1%.

LORRI does not have a shutter. Whenever LORRI is active, the CCD is exposed to whatever scene is in the FOV. The clocking of the CCD includes a "frame scrub," followed by exposure to the scene for the commanded integration time, followed by a "frame transfer" in which the CCD rows are sequentially transferred from the optically active area to the image storage region, followed by a readout of the image storage region to the downstream electronics, which convert the detected electrons to DNs. The digitized image is then transferred to the spacecraft's solid state recorder (SSR). The spacecraft's command and data handling (CDH) computer can either losslessly compress the full image, lossy compress the full image, or window and losslessly compress arbitrarily selected portions of the image. When commanded to do so, the CDH computer can send selected images from the SSR to the spacecraft's telecommunications hardware for downlink to the antennas of NASA's deep space network (DSN). For observations conducted in the Kuiper Belt (i.e., when the heliocentric distance is ⩾30 au), data downlink rates are typically ∼2 kbps when both of the redundant transmitters are used, or ∼1 kbps when only a single transmitter is used.

LORRI does not have any color filters. Instead, LORRI maximizes sensitivity by providing panchromatic imaging over a wide bandpass: 435–870 nm at the 50% throughput points and 360–910 nm at the 10% throughput points. Images can be taken at a rate of up to once per second, or at any commanded cadence longer than that. Manual exposure times can be commanded from 0 ms to 64,967 ms in 1 ms increments.[6] We recently (2019 July) discovered an error in the exposure times reported by the LORRI flight software. As a consequence, the actual exposure time is ∼0.6 ms longer than reported. This error is insignificant for most LORRI images, but it is important for many of the LORRI images taken during the

[6] New LORRI flight software was uploaded in 2019 July that enabled exposure times up to 64,967 ms. Prior to that, the longest available exposure time was 29,967 ms. Observations taken in 2019 September have verified nominal performance with exposure times of 64,967 ms.

Jupiter flyby, when the commanded exposure times were generally $\leqslant$10 ms. We note also that using the actual exposure time is important for correcting the smear produced during the frame scrub and frame transfer process, as described later in more detail. The LORRI data will be re-processed to account for this error in the exposure times for a future delivery to the Planetary Data System archive.

A flexible autoexposure mode is available whenever the scene being imaged has unknown intensities, but autoexposure can only be used for exposure times $\leqslant$967 ms. Although we exercise the autoexposure capability at every annual checkout, we have generally preferred to use two different *manual* exposure times that span the dynamic range of interest, rather than relying on autoexposure mode for in-flight observations of targets with unknown, or poorly characterized, brightnesses.

A "trigger" mode is also available that enables LORRI to determine autonomously when a target has entered the FOV, via analysis of a 32-bin histogram of the image, and then send images to the spacecraft for a specified duration after the trigger condition has been satisfied. Trigger mode was developed in 2011 and required uplinking to the spacecraft new LORRI flight software. The primary potential use of trigger mode was to enable taking many (tens to hundreds) 1×1 images during the Pluto flyby as the LORRI FOV was scanned across Pluto and Charon and their very large pointing error ellipses without filling up the solid state recorder with many dozens of blank sky images. Although trigger mode was tested extensively on the ground using the LORRI engineering model, and trigger mode also worked successfully during an in-flight test scanning the LORRI FOV across a bright star, no in-flight test of an *extended* target could be identified that mimicked the conditions of the Pluto flyby. For that reason, the *New Horizons* Project decided *not* to use trigger mode during the Pluto flyby. Trigger mode was also not used during the *New Horizons* spacecraft flyby of the Kuiper Belt object 2014 MU_{69} (hereafter "MU69") because that target was so faint that the necessary trigger condition could not be satisfied with the coarse (32 bins) image histogram available.

The *New Horizons* spacecraft has two main guidance and control (GNC) states: either spinning at $\sim$5 rpm about an axis approximately aligned with the high gain antenna and the LORRI boresight, or 3-axis stabilized mode. When operating in 3-axis mode, which is usually the case during science observations for the remote sensing instruments, the *New Horizons* spacecraft fires hydrazine thrusters to maintain the pointing within a specified attitude "deadband." (Owing to power constraints, *New Horizons* does not have reaction wheels to stabilize the pointing.) The deadbands used during LORRI 1×1 observations are either $\pm 51\farcs6$ or $\pm 103''$, with thruster firings approximately every 3 s and every 6 s, respectively. Typical pointing drift rates during 3-axis observations are $\sim 5'' \, s^{-1}$; typical 1×1 exposure times are 0.10–0.15 s during science observations to limit pointing smear to $\leqslant$1 pixel.

Shortly after launch, a new 3-axis pointing mode, called "relative control mode" (RCM), was developed to enable long duration exposures in 4×4 format. In RCM, the thrusters are fired $\sim$80 times per minute to keep the LORRI boresight at a fixed inertial pointing location to an accuracy of $\pm 2''$ (1σ) for exposure times up to $\sim$65 s. RCM has enabled LORRI deep imaging observations that can reach $V \approx 20.2$ with $S/N = 5$ in a single 65 s image for targets with solar-type spectral energy distributions (SEDs) in relatively sparse fields. Figure 5 shows a composite LORRI 4×4 image of the MU69 background field produced by combining 96 individual 30 s exposures, which reaches $V \approx 22$ (S/N=5) in the regions with relatively few background stars.

For most LORRI science and calibration observations, the boresight is pointed at the target of interest, the CCD is exposed for the commanded duration (typically 100–150 ms), and the CCD is read out after the exposure is finished. In this case, the exposure times are long enough to provide excellent signal-to-noise ratios (S/Ns), but they are short enough to provide high resolution imaging performance without significant degradation as the target drifts within the pointing deadband. Figure 6 shows an example of this type of observation taken during the approach to Pluto in 2015 July. Deconvolution (see later discussion), which restores signal to the core that was originally spread into the PSF wings, was applied to sharpen the image and achieve nearly diffraction-limited resolution.

However, during flyby encounters LORRI images are also frequently taken while the spacecraft is scanning the Ralph instrument across the target and its error ellipse. This mode enables simultaneous LORRI and Ralph observations, but the LORRI exposure times must be much shorter to prevent excessive smear during the scan. Typically LORRI images are taken either every second, or every 3 s, during such scans, and the overlapping fields of view enable co-adding the images to recover better S/N. In addition, deconvolution techniques can be employed to recover better optical resolution, approaching that of the equivalent non-scanned observations. Figure 7 shows an example of a composite LORRI image obtained during a Ralph-MVIC scan across the middle of Pluto near the time of closest approach. This particular scan produced the highest resolution imaging of Pluto obtained during the flyby.

A detailed description of LORRI and its use on *New Horizons* can be found in Cheng et al. (2008). Engineering details on the construction of LORRI can be found in Conard et al. (2005). The ground-based calibration of LORRI is described in Morgan et al. (2005). LORRI's performance through the Jupiter flyby is described in Noble et al. (2009), and LORRI's performance during the Pluto flyby is described in Conard et al. (2017). LORRI's in-flight straylight performance is described in Cheng et al. (2010), and a detailed comparison of LORRI's optical design and its actual performance is described in McMichael & Bentley (2012). Zemcov et al. (2017) describes attempts to measure the extragalactic background optical light with LORRI, and Zemcov et al. (2018) describe LORRI's potential future uses

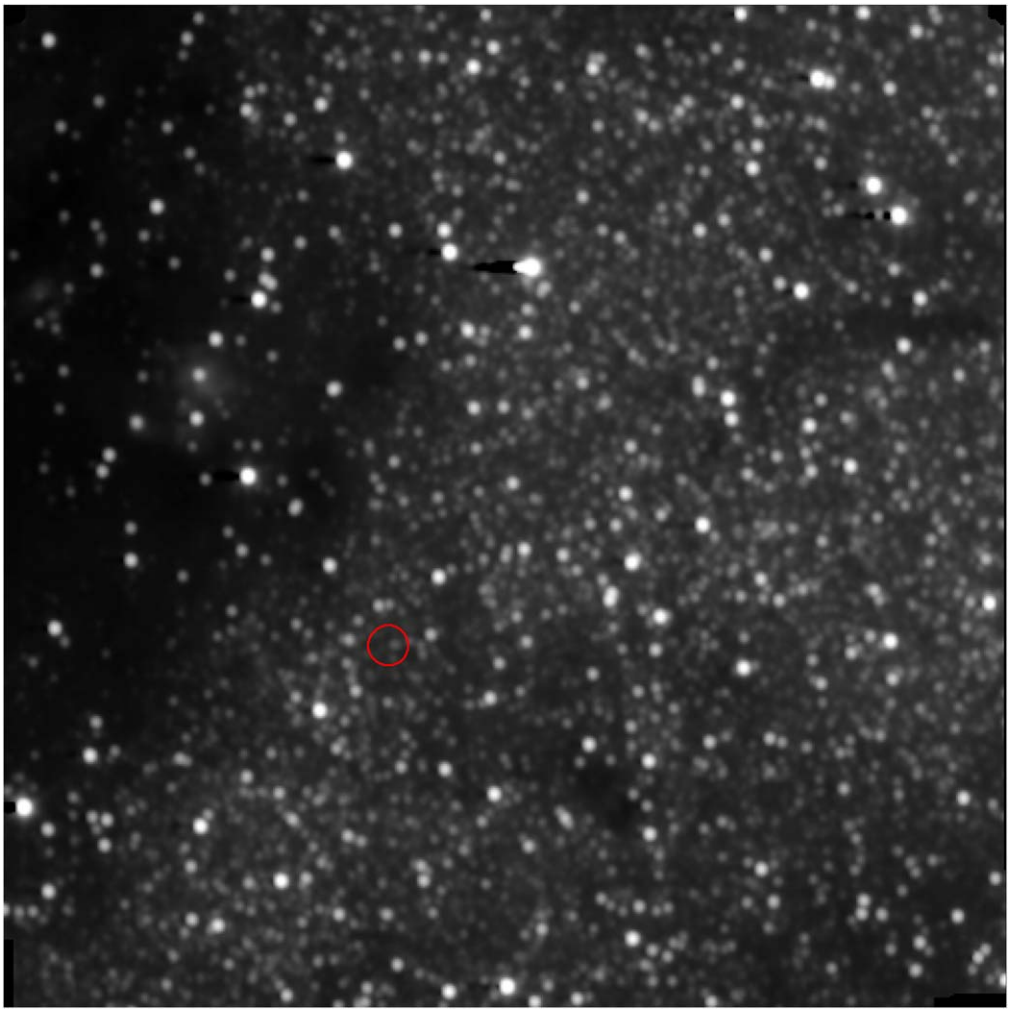

Figure 5. This deep LORRI image of the MU69 background field was produced by combining 96 individual 30 s images taken on 2017 September 21. Celestial north is up, and east points to the left. The pixels are subsampled by a factor of two (using sinc function interpolation) to remove the pixelated appearance of the raw 4 × 4 image. A hyperbolic sine (sinh) intensity stretch (similar to logarithmic but better behaved near 0) ranging from −1 to 3500 DN is used to show the full dynamic range of the image. The brightest stars are saturated and have black tails due to amplifier undershoot. The red circle is centered on the predicted location of MU69, but MU69 was fainter than LORRI's sensitivity limit, which is estimated to be $V \approx 22$ in this composite. This composite image was used as a template that could be subtracted from LORRI images of MU69 taken in late-2018, thereby removing nearby stars and enabling the detection of MU69 for optical navigation and deep searches for satellites and dust in the vicinity of MU69.
(A color version of this figure is available in the online journal.)

for various astrophysical objectives. Below we focus on the results from the in-flight LORRI calibration observations, their trending with time over the entire *New Horizons* mission to date, and how the calibration results are used to derive the various photometry keywords needed to transform LORRI images from engineering units to absolutely calibrated scientific units.

2. Calibration Steps

Before discussing the in-flight LORRI calibration program and its results, we first describe the steps in the LORRI calibration pipeline, which is the software that removes instrumental artifacts in the raw images and creates the calibrated images that can be used for scientific analysis. The calibration pipeline makes use of reference files that are derived from either ground or flight calibration measurements, as described further below. Critically, the pipeline populates various photometry FITS header keywords based on the results from LORRI observations of absolute calibration standard stars, as discussed in Section 3.

2.1. Bias and Dark Subtraction

After the LORRI aperture door was opened on 2006 August 29, the CCD temperature has typically been within a

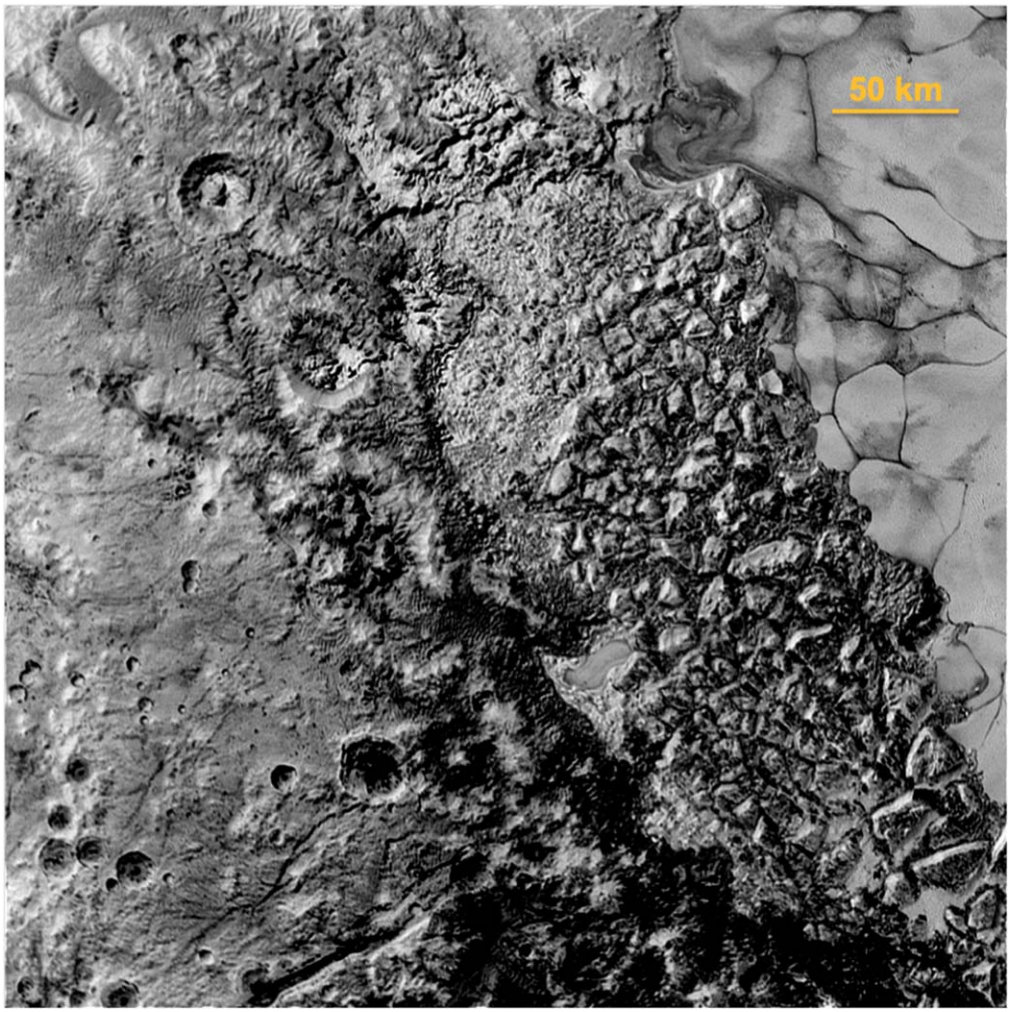

Figure 6. This is a deconvolved LORRI image of the al-Adrisi mountains on Pluto taken on 2015 July 14 when the spacecraft was 78,600 km from the surface (0.390 km pixel^{-1}). The exposure time was 0.15 s, which is in the typical range used for science observations when LORRI is the prime instrument, with its boresight fixed relative to the target. The region to the right of the frame is the northwest corner of Sputnik Planitia (SP), a giant ice sheet composed primarily of N_2 that displays a geometrical pattern attributed to rising (near the center of a pattern) and falling (at the boundaries of the patterns) icy material heated from below. The mountains are the blocky structures at the edge of SP and are thought to be giant water icebergs floating in the nitrogen ice. Many other interesting geological features are evident in this image, as discussed in Moore et al. (2016).
(A color version of this figure is available in the online journal.)

few degrees of −81 °C. At this temperature, the CCD dark current is usually negligible for most LORRI observations. The process used to subtract the CCD electronic offset signal (which is called the "bias" level and is used to prevent sending negative analog signals to the analog-to-digital converter) automatically includes any dark current that may be present. From a series of long exposure time images (up to 64.967 s) taken during a test in 2019 July when the CCD temperature was −81 °C, we determined an *upper limit* for the dark current in 1 × 1 pixels of 0.0019 DN s^{-1} pixel^{-1}, corresponding to 0.040 *e* s^{-1} pixel^{-1} at the nominal gain of 21 *e* pixel^{-1}, which is approximately 10 times larger than the dark current calculated using data from the CCD manufacturer's specification sheet. During long exposure (⩾10 s) 4 × 4 images obtained during flight, "warm" pixels are clearly detected with elevated dark currents (up to a few DN in magnitude, after subtraction of the median bias plus dark level). The locations of these "warm" pixels vary over time, but they never comprise more than 1% of the total number of pixels in the image.

The bias level is a function of the temperature of the FPE board. From the ground calibration data, we derived that the bias level for 1 × 1 images is given by:

$$\text{bias} = 503.968\ (\pm 0.549) + 1.239\ (\pm 0.015) * T_{\text{board}} \quad (1)$$

where "bias" is the bias level in DN and T_{board} is the FPE board temperature. For 4 × 4 images the bias level is typically ∼4 DN larger. LORRI in-flight images have bias levels that are

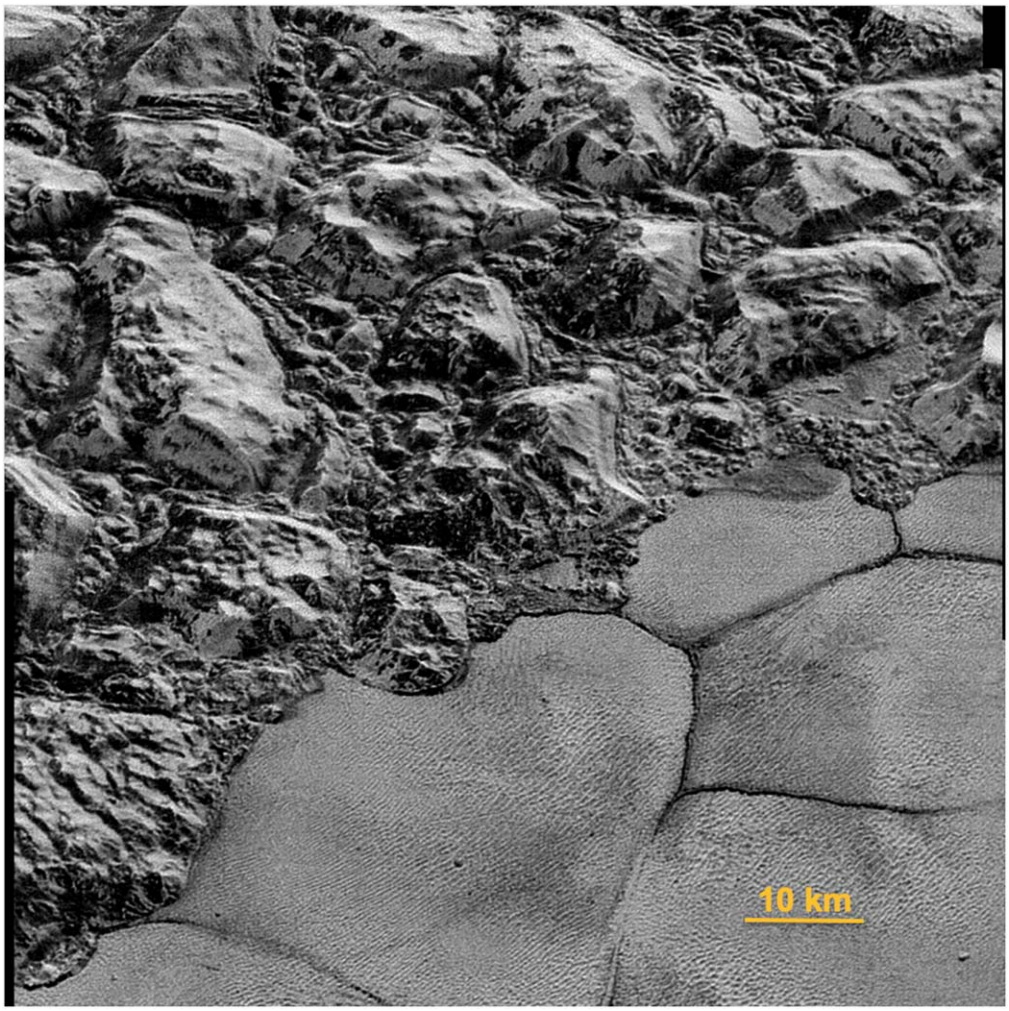

Figure 7. This is a deconvolved LORRI image showing even finer detail on Pluto's surface, in this case the border between the Sputnik Planitia ice sheet (the smooth geometrical patterns below and to the right) and the chaotic terrain called the al-Adrisi mountain range. This image was taken on 2015 July 14 when the spacecraft was 17,000 km from the surface (0.084 km pixel^{-1}). The LORRI images were taken while scanning the MVIC imager across Pluto at 1000 μrad s^{-1}, which required using LORRI exposure times of only 0.010 s to minimize pointing smear during the scan. Although LORRI uses a standard frame transfer CCD, while MVIC uses a CCD in time delay integration (TDI) mode ("push broom mode"), LORRI's high sensitivity enabled its use during scanning observations.
(A color version of this figure is available in the online journal.)

generally consistent with this formula. After the LORRI aperture door was opened on 2006 August 29, the FPE board temperature has typically been in the range 23 °C–29 °C.

We have recently (in 2019) noticed that the bias level may also display a "start-up" feature, whereby the bias level starts at a slightly higher value and gradually plateaus to its expected value over the course of several minutes. This behavior is still being characterized, but the magnitude of the effect is at the sub-DN level, which is inconsequential for most *New Horizons* science applications. We do, however, want to understand this effect better because it will likely affect LORRI's ability to accurately measure the extragalactic background light (Zemcov et al. 2017).

As implemented in the LORRI pipeline, the bias+dark subtraction is a two-step process. First, the overall bias+dark level for an image is subtracted from the raw ("Level 1") image. Specifically, for 1 × 1 images (i.e., Level 1 files having 1028 × 1024 pixels) the median intensity of the pixels in columns 1024−1027 of the Level 1 image (corresponding to columns 1032−1035 of the CCD, which are in a portion of the CCD not directly illuminated) is subtracted from each pixel in the Level 1 image. For 4 × 4 images (i.e., Level 1 files having 257 × 256 pixels), the median intensity of pixels in column 257 (which is the re-binned version of CCD columns 1032–1035 in the 1 × 1 image) is subtracted from each pixel in the Level 1 image. Since the bias columns also accumulate CCD dark

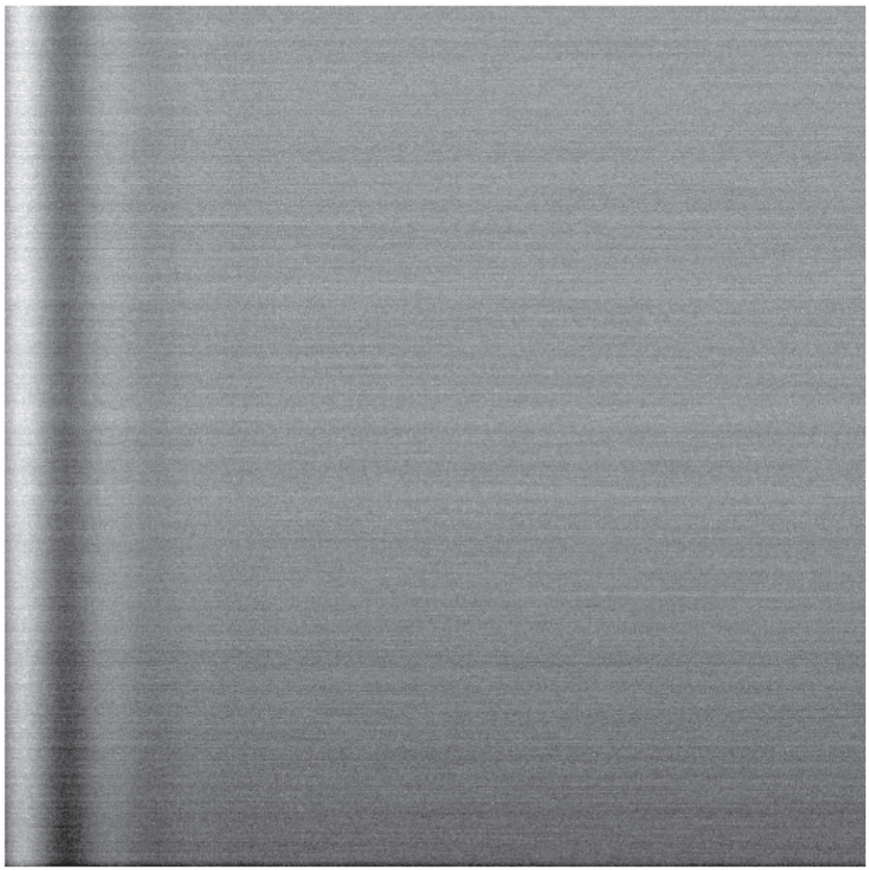

Figure 8. This "delta-bias" image, which shows the pixel-to-pixel variations in the bias level, was created by combining 100 1 × 1 images, each with an exposure time of 0 ms, taken before the aperture door was opened. The image is displayed using a linear intensity stretch ranging from −1 to +1 DN.

current, the median dark current is also removed during this step.

The simple median of the pixels in the inactive region may not provide the best estimate of the global bias+dark level, if the distribution of pixel values is distorted by multiple cosmic rays, or other artifacts. We have recently investigated an alternative approach, using fits to the well-defined peak in the histogram of the pixel values as the bias level estimate. Although this technique may indeed provide a better estimate of the true bias level, we have found that the differences with the median values are typically $\leqslant$0.3 DN, which is smaller than the typical electronics noise level ($\sim$1.1 DN). We have decided to stick with the simple median for the near-term because this approach is more robust (i.e., not subject to subtle computational issues) and easier to implement. However, we may eventually employ a different technique to enable achieving the highest possible sensitivity for the most demanding observations.

After this global bias+dark level is subtracted, a "delta-bias" (sometimes called a "superbias") image is then subtracted from the image. The delta-bias image captures the pixel-to-pixel variations in the bias and was created by averaging 100 1 × 1 bias frames (i.e., images with exposure times of 0 s) taken in-flight on 2006 July 30 with the main aperture door closed, as part of a LORRI in-flight calibration activity (Figure 8). The delta-bias image for 4 × 4 format images was obtained by simple re-binning of the average 1 × 1 delta-bias image. Although 4 × 4 bias images were obtained in 2006 April and May, those were contaminated by light passing through the small circular window ($\sim$2.54 cm in diameter) in the main aperture door. This window was placed in the aperture door to permit LORRI to have some imaging capability in case the main aperture door did not open. The light passing through this small window was too weak to affect the 1 × 1 bias images, but could be faintly seen in the 4 × 4 bias images.

Bias images in both 1 × 1 and 4 × 4 format have been taken at least once per year during the entire *New Horizons* mission. No systematic change in the bias images has ever been seen. LORRI images (both bias images and regular images) sometimes exhibit a small even–odd column signal offsets ("jail bars"), but the effect is generally $\leqslant$0.5 DN in magnitude, which is smaller than the typical electronics noise ($\sim$1.1 DN). We have not been able to correlate the appearance of the jail bars with any

particular instrument parameter (e.g., there is no correlation with the temperatures of the CCD or the electronics). But if they are present, the jail bars are usually present in an entire set of images taken near the same time. In that case, the jail bars can be removed fairly easily with standard image processing techniques (e.g., by creating a template image with the jail bar pattern and subtracting that from the original image).

Individual LORRI images in both formats also display a low-level ($\leqslant$1 DN) horizontal (i.e., row-based) pattern that is apparently associated with the injection of non-random noise during the CCD frame transfer process. This "horizontal striping" is always present but is usually only evident when large portions of the image have little or no signal (e.g., when observing sparse star fields). The stripes change locations from frame-to-frame producing a non-random noise pattern across each image. This pattern can be removed from an individual image with standard image processing techniques (e.g., by subtracting a median smoothed, or robust average, level from each row).

The electronics noise is measured by subtracting one bias frame from another and examining the residuals. This technique has been applied throughout the mission, and the results demonstrate that the electronics noise has remained virtually the same for the entire mission ($\sim$1.1 DN) for both CCD formats.

2.2. Desmear

As already mentioned above, LORRI does not have a shutter. Thus, the target being observed illuminates the active region of the CCD whenever LORRI is pointed at the scene. In particular, the CCD continues to record the scene as the "scrub" is performed (before the nominal start of the exposure) and as charge is transferred from the active portion to the storage area (after the nominal end of the exposure). Both of these processes result in a smearing of the observed scene along a CCD column.

The smear process can be visualized as pulling a sheet of light sensitive film, whose size is exactly the size of the CCD's active area, uniformly across a scene whose size is also exactly the size of the CCD's sensitive area. The flush begins as the film is pulled across the scene starting from the top of the CCD (i.e., starting at the highest CCD row) until the film exactly covers the full scene. The total flush time is the duration of that process, and the rate of motion, which is also the row transfer time, determines how much signal from pixels at *higher* rows is transferred to any particular pixel in the same column. After the flush process is completed, the film stays in place for the commanded exposure time, and each pixel accumulates signal only from the scene imaged at that pixel. After the exposure is completed, the film is pulled in the same direction as before, but this time each pixel will accumulate signal from the scene in rows below that pixel as the film is moved to the image storage region of the CCD, which is also completely outside the illuminated scene. The total transfer time is the duration of that process, and the rate of rate of motion during the transfer determines how much signal from pixels at *lower* rows is transferred to any particular pixel in the same column. All of the pixels in the CCD storage region are then transferred row-by-row to the CCD serial readout register, where the analog signals are amplified and then digitized.

For images with no over-exposed pixels and that have fixed pointing during the exposure, the smear can be essentially completely removed using the algorithm described in Cheng et al. (2008). Once a pixel is over-exposed, however, information on its true intrinsic level is lost and the smear correction will be incomplete for that column of the image. As the de-smear algorithm works on a column by column basis, any significant motion of the camera during the exposure in the row direction (i.e., perpendicular to the columns), as can occur when LORRI is used in ride-along mode with the *New Horizons* MVIC or LEISA instruments, may also limit the accuracy of the correction. Of course, the de-smear correction cannot remove the extra shot-noise associated with the smeared light. For long exposures this is only a modest effect, but for images of extended targets with short exposure times (i.e., similar to, or smaller than, the total frame transfer time of $\sim$12 ms), the signals generated during the scrub and transfer processes are comparable to, or even larger than, the signal levels accumulated during the nominal exposure time. In this case, the shot noise from the smear signal produces significant degradation of the S/N. For example, when the signal accumulated during the exposure time is comparable to that accumulated during the scrub and transfer, the S/N is reduced by approximately $\sqrt{2}$ compared to the case when frame transfer smear is negligible.

The de-smear algorithm described in Cheng et al. (2008) is complex and computationally intensive. Given the sparse nature of the "error matrix" used in that formulation, we identified a technique for speeding up the calculations by a factor of $\sim$10 compared to performing the matrix multiplications given in Cheng et al. (2008). This faster technique, which produces results essentially identical to those using the full matrix multiplication, has been used in the LORRI data pipeline since 2014.

We have recently investigated two alternative formulations for the desmear step, which are simpler and easier to implement than the algorithm given in Cheng et al. (2008). One of the algorithms (Owen et al. 2019, in press) adopts approximations to accelerate the computation by avoiding matrix operations. Another algorithm, discussed further below, is exact but involves a matrix inversion for each image. The new algorithms are still being evaluated and must be tested extensively before either can be used in the LORRI calibration pipeline.

2.2.1. An Exact Simple De-smear Algorithm

We are presently investigating an alternative algorithm for the de-smear step, which is simpler and easier to implement than the algorithm given in Cheng et al. (2008). As with the Cheng et al. (2008) approach, the new algorithm is applied on a per column basis, since the smeared charge associated with any pixel stays within its column. The solution is derived with a single matrix multiplication that transforms the column of data values as generated by LORRI to a column of pixel values corrected for charge-transfer smear.

For any column of pixels in the LORRI CCD, neglecting dark current, the rate at which signal is accumulated in a LORRI CCD pixel within that column can be written as:

$$\frac{S_k}{t_{\rm exp}} = \sum_{i,i>k}^{n} R_i\, I_i\, \frac{t_{\rm scrub}}{t_{\rm exp}} + \sum_{i,i<k}^{n} R_i\, I_i\, \frac{t_{\rm transfer}}{t_{\rm exp}} + R_k\, I_k \qquad (2)$$

where:

S_k is the measured signal in a pixel in row k (electrons, or "e").
R_x is the intrinsic responsivity of pixel x (($e\,{\rm s}^{-1}$ pixel^{-1})/(photons s^{-1} pixel^{-1})).
I_x is the input photon flux at pixel x (photons s^{-1} pixel^{-1}).
$t_{\rm exp}$ is the total exposure time (s), which is the commanded time plus 0.6 ms.
$t_{\rm scrub}$ is the CCD row transfer time during the frame scrub (s).
$t_{\rm transfer}$ is the CCD row transfer time during the frame transfer (s).
n is the number of rows in the image (1024 for 1 × 1 images and 256 for 4 × 4 images).

The first term on the right-hand side of the equation represents the smear contribution to the observed signal from pixels in the same column, but at *larger* row numbers compared to the pixel of interest, and is accumulated during the frame scrub process. The second term on the right-hand side of the equation represents the smear contribution to the observed signal from pixels in the same column, but at *smaller* row numbers compared to the pixel of interest, and is accumulated during the frame transfer process. The third term is the actual desired quantity, the signal accumulated at the pixel of interest during the commanded exposure time.

Equation (2) can be recast as a matrix equation:

$$D_i = \sum_{j=1}^{n} g_{ij}\, F_j \qquad (3)$$

$$\rightarrow \boldsymbol{D} = \boldsymbol{G}\,\boldsymbol{F} \qquad (4)$$

where in any CCD column:

D_i is the detected signal (including smear) at row i (DN).
F_j is the true signal (not including smear) at row j (DN).
g_{ij} are coefficients determined as described below.

The coefficients of $\boldsymbol{G}$ are analogous to, but not identical to, the ϵ coefficients in the smear formulation of Cheng et al. (2008). For LORRI, the frame scrub takes a total of 12.15 ms, which means each row transfer ($t_{\rm scrub}$ above) takes 0.0119 ms for 1 × 1 images and 0.0474 ms for 4 × 4 images. The frame transfer takes 11.12 ms, which means each row transfer ($t_{\rm transfer}$ above) takes 0.0109 ms for 1 × 1 images and 0.0434 ms for 4 × 4 images. Note that $g_{ij} = 1$ when $j = i$, $g_{ij} = t_{\rm scrub}/t_{\rm exp}$ when $j > i$, and $g_{ij} = t_{\rm transfer}/t_{\rm exp}$ when $j < i$.

In summary, the measured count rates for the pixels in a column (represented by the column matrix $\boldsymbol{D}$) can be represented by the matrix multiplication of the smear matrix and a column matrix of the actual count rates (i.e., $\boldsymbol{F}$, the count rates after the smear contributions have been removed). Thus, the desmear problem reduces to finding the inverse of the smear matrix:

$$\boldsymbol{F} = \boldsymbol{G}^{-1}\,\boldsymbol{D}. \qquad (5)$$

Note that the matrix inversion need only be performed once for each image because the smear matrix is identical for each column in the image. In fact, the smear matrix depends only on the ratios $t_{\rm scrub}/t_{\rm exp}$ and $t_{\rm transfer}/t_{\rm exp}$. In principle, the matrix inversion could be performed in advance for each exposure time employed, in which case the matrix inversion within the calibration pipeline could be replaced by a simple lookup of the appropriate inverted matrix, which could be stored in a reference file directory (e.g., similar to what is done for the delta-bias and flat field).

2.3. Flat-field

Flat-fielding refers to the process of removing the pixel-to-pixel sensitivity variations in the image. An exposure obtained by illuminating the LORRI aperture uniformly with light is called a flat-field image. During ground calibration testing, flat-fields were obtained by using an integrating sphere to provide uniform illumination (Morgan et al. 2005). The light source was a xenon arc lamp with a spectrum similar to that of the Sun. The absolute intensity of the input illumination was measured using a calibrated photodiode. For the panchromatic case, which is the one most relevant for flat-fielding LORRI images, the light from the xenon lamp was unfiltered. Flat-field images were also obtained by passing the light through bandpass filters centered at five different wavelengths spanning the range over which LORRI is sensitive, prior to injection into the reference sphere, to estimate the sensitivity of the flat-fields to the spectral distribution of the source. The spatial patterns in the flat-field images change significantly with wavelength. However, the variation in panchromatic flat-fields caused by differences in the spectral distribution of the illumination source are much less significant. Indeed, panchromatic flat-field images produced using a tungsten lamp were virtually indistinguishable from those produced by the xenon lamp. Flat-fields were obtained at four different sets of thermal environments (at

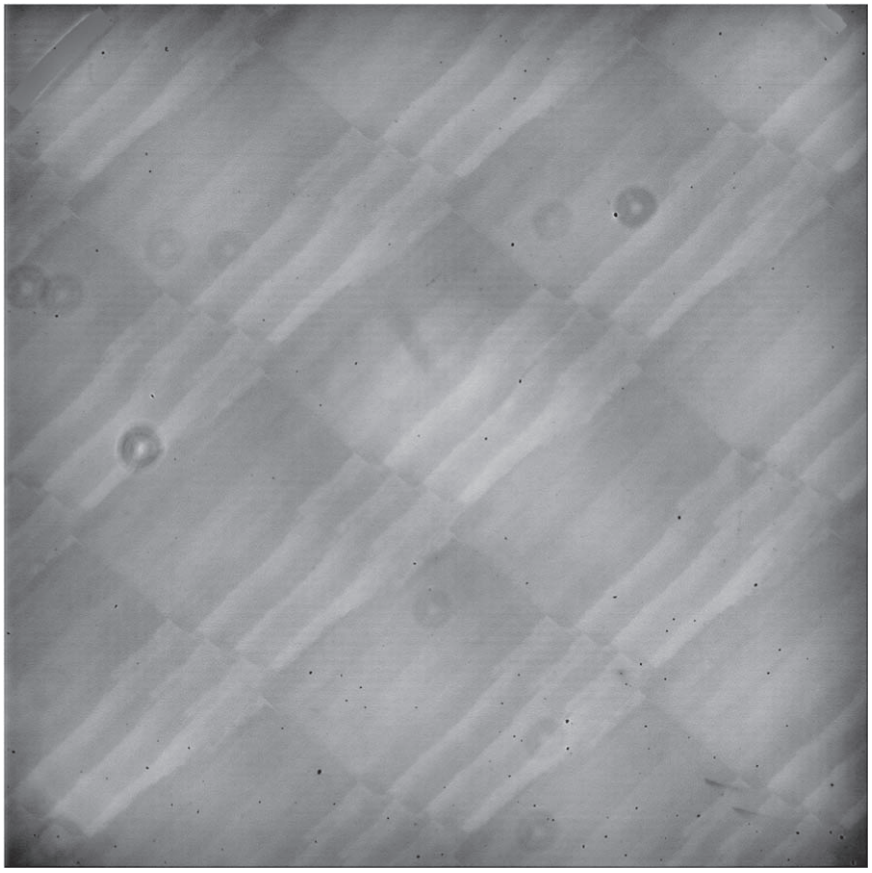

Figure 9. The LORRI 1 × 1 flat-field image used in the calibration pipeline is displayed using a linear intensity stretch from 0.95 to 1.05. This flat was produced by co-adding 100 panchromatic images taken during the ground calibration (Morgan et al. 2005). The diagonal-shaped structures are intrinsic to the CCD. The small black spots are paint flakes that rained down on the CCD during the LORRI vibration test. The larger donut-shaped features are probably out-of-focus flakes (e.g., flakes on one of the lens surfaces). The flakes themselves were likely produced when the last lens in the lens assembly was replaced because of a chipped edge, during the latter stage of the telescope assembly. Most of the flakes were blown off the CCD after the vibration test, but many remained essentially stuck to the CCD and have not moved over the entire duration of the *New Horizons* mission (as documented from images of the internal calibration lamp). The dark streaks in the lower right quadrant were apparently produced when a camel hair brush was moved across the CCD (in an attempt to remove the flakes). There are two diagonal-shaped artifacts, one in the upper left (the larger one) and one in the upper right, which are the residuals from our attempt to remove the stray light seen in those regions.

standard laboratory room temperature, and at the lowest, nominal, and highest temperatures predicted for in-flight conditions), but no significant variations in the flat-field images were detected.

No suitable flat field astronomical target was available after launch. The flat-field reference file used in the LORRI calibration pipeline was produced by averaging 100 flat-field images taken at room temperature during ground testing using the xenon arc lamp as the light source, debiasing and desmearing the average image as described earlier, and normalizing the intensities in the active region to a median value of 1 (Figure 9). If S (units are DN) is an image of a target that has already been desmeared and debiased, and if FF is the reference flat-field image, then the flat-fielded (i.e., photometrically corrected) target image (C; units are DN) is given by $C = S/\mathrm{FF}$.

The LORRI flat-field has been monitored throughout the *New Horizons* mission by taking exposures with onboard "cal lamps," which refer to two small tungsten filament lamps mounted on opposite sides of the CCD, in close proximity to the CCD. The primary function of these onboard lamps is to provide illumination of the CCD during "functional" tests, which verify basic operation of the CCD and its electronics, but *not* the OTA. The illumination provided by the lamps is highly non-uniform spatially (see the top row of Figure 10) but is highly stable over time. The temporal stability of the lamps has been monitored annually throughout the mission. Ratios of lamp images taken at different times provide a sensitive measure of the stability of the lamps (see the bottom row of Figure 10). The histogram for the lamp #2 ratio image in Figure 10 is a bit tighter than the histogram for the

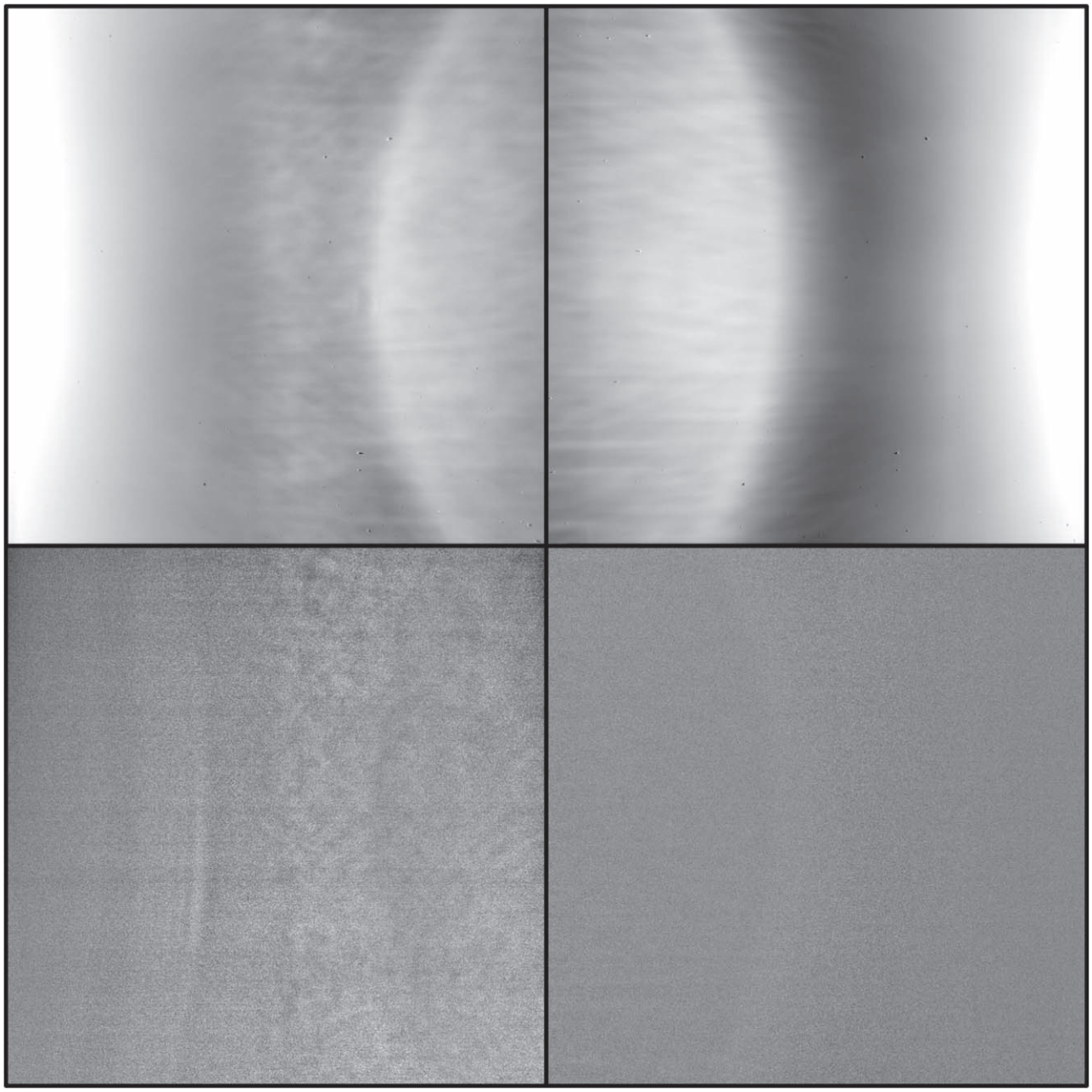

Figure 10. Two "cal lamps" provide illumination of the LORRI CCD during in-flight functional tests. The upper left frame shows a 1×1 CCD image during illumination from lamp #1, and the upper right frame shows a 1×1 image during illumination from lamp #2, both displayed using a hyperbolic sine intensity stretch to better show the dynamic range in the images. Both images were taken during ACO-1 on 2007 October 29, and both show the highly non-uniform light distribution produced by these lamps. The lamps illuminate multiple particles that rained down on the CCD during a vibration test. The oblique illumination across the CCD produces shadows for some of the images of these particles. Although highly non-uniform spatially, the illumination from the lamps has been stable over time. The bottom frames show the ratios of the ACO-1 lamp images to the ACO-8 lamp images taken on 2014 July 5, for lamp #1 (lower left frame) and lamp #2 (lower right frame). Both ratio images are displayed using a linear intensity stretch ranging from 0.9 to 1.1 (i.e., a total range of $\pm 10\%$).

lamp #1 ratio image, but both lamps show remarkable temporal stability with the average, median, and most common ratio values within 0.1% of unity for both lamps. Furthermore, these lamp images demonstrate that he particles on the CCD have not moved over the entire duration of the mission (i.e., their locations are fixed in CCD coordinates),

Table 2
LORRI Photometry Keywords

Keyword	Value (1 × 1)	Value (4 × 4)
RSOLAR	2.349×10^5	4.092×10^6
RPLUTO	2.270×10^5	3.955×10^6
RCHARON	2.318×10^5	4.039×10^6
RJUPITER	2.069×10^5	3.605×10^6
RMU69	2.499×10^5	4.354×10^6
RPHOLUS	2.724×10^5	4.746×10^6
PSOLAR	9.533×10^{15}	1.038×10^{16}
PPLUTO	9.214×10^{15}	1.003×10^{16}
PCHARON	9.410×10^{15}	1.025×10^{16}
PJUPITER	8.397×10^{15}	9.144×10^{15}
PMU69	1.104×10^{16}	1.105×10^{16}
PPHOLUS	1.106×10^{16}	1.204×10^{16}

Note. The keywords starting with "*R*" are diffuse target sensitivity keywords and their values have units of (DN s^{-1} $pixel^{-1}$)/(erg cm^{-2} s^{-1} $Å^{-1}$ sr^{-1}). The keywords starting with "*P*" are point target sensitivity keywords and their values have units of (DN s^{-1})/(erg cm^{-2} s^{-1} $Å^{-1}$). For point targets the signal refers to values integrated over the entire instrumental PSF.

which means the flat-field correction employed by the calibration pipeline accurately removes any artifacts they might create during observations.

2.4. Conversion to Scientific Units

The software pipeline that performs the calibration steps defined above does not perform the conversion from DN to physical units because that conversion requires knowledge of the SED of the target. (The SED is related to the "color" of the target in standard astronomical usage.) Instead, various LORRI FITS header keywords ("photometry" keywords) are provided that allow users to convert from DN to physical units depending on the spectral type and spatial distribution (diffuse versus point source) of the target. Photometry keywords are provided for targets having spectral distributions similar to Pluto, Charon, Pholus, Jupiter, MU69, and the Sun. The units adopted for the radiance (also called "intensity") of diffuse targets are erg cm^{-2} s^{-1} $Å^{-1}$ sr^{-1} . The units adopted for the irradiance (also called "flux") of point (i.e., unresolved) targets are erg cm^{-2} s^{-1} $Å^{-1}$. The latest (i.e., current) values of the photometry keywords are provided in the header of the calibrated (called "Level 2") FITS file for the image being analyzed. The photometry keywords derived from the in-flight calibration campaign conducted in 2016 July, using the star HD 37962 (with a solar-type SED) as the absolute calibration standard, is provided in Table 2. All of these keywords enable conversion of raw signals in engineering units to absolute signals at the so-called "pivot" wavelength ($\lambda_{\rm pivot}$), which is one way of characterizing the "effective" wavelength for a broadband optical instrument. The pivot wavelength is defined as:

$$\lambda_{\rm pivot} = \sqrt{\frac{\int {\rm QE} * \lambda \, d\lambda}{\int {\rm QE}/\lambda \, d\lambda}} \tag{6}$$

where "QE" is the total system quantum efficiency (see the next section). The pivot wavelength for LORRI is calculated to be 6076 Å.

Table 3
LORRI Color Corrections

Spectral Type	CC
O, B, A stars	−0.060
F, G stars	+0.000
K stars	+0.400
M stars	+0.600
Pluto	−0.037
Charon	−0.014
Jupiter	−0.138
Pholus	+0.161
MU69	+0.067

Note. For targets of the specified spectral type, CC provides the color correction term in the formula used for converting LORRI count rates (DN s^{-1}) to Johnson *V* magnitude.

For convenience to users, we provide a prescription for converting LORRI signal rates to standard *V* magnitudes in the Johnson photometric system:

$$V = -2.5 \log(S/t_{\rm exp}) + {\rm ZPT} + {\rm CC} - {\rm AC} \tag{7}$$

where *V* is the magnitude in the standard Johnson *V* band (i.e., specifies the target's flux at 5500 Å), *S* is the measured signal in the selected photometric aperture (DN), $t_{\rm exp}$ is the exposure time (s), ZPT is the photometric zero-point (18.78 for 1 × 1 and 18.88 for 4 × 4), CC is a color correction term (as specified in Table 3), and AC is an aperture correction term to convert from the flux collected in a specified synthetic aperture to the total flux integrated over the LORRI PSF. The CC terms listed in Table 3 were calculated using SEDs for the listed spectral types. For the specified stellar types, we used SEDs downloaded from the exposure time calculators at the Space Telescope Science Institute. For the other listed spectral types, we used SEDs adopted by the *New Horizons* team, which are based on published spectra. For typical LORRI observations of point sources, the S/N is optimized by integrating over a circular aperture with a radius of 5 pixels (1 × 1 format) or 3 pixels (4 × 4 format), in which case AC is either 0.10 or 0.05, respectively.

We provide here two examples showing how to convert from engineering units to physical units: one for a diffuse target and one for a point (i.e., unresolved) target. Consider a diffuse target whose spectrum is similar to that of Pluto's globally averaged SED. In this case, the RPLUTO photometry keyword in the header of the Level 2 (i.e., calibrated) file should be used

Table 4
LORRI in-flight Calibration Observations

Cal ID (1)	Date (2)	SAP ID (3)	Target (4)	Objective (5)
ACO-0	2006 Apr 23, 24	025	N/A	Bias images, CR monitoring (4 × 4)
	2006 May 23	025	N/A	Bias images, CR monitoring (4 × 4)
	2006 Jul 30	006	N/A	Bias images, CR monitoring (1 × 1)
	2006 Aug 29	007	M7	After door opened for first time
	2006 Aug 31	010	M7	Optical performance, Linearity, Pointing drift
	2006 Aug 31	018	M7	Coalignment measurements with MVIC
	2006 Sep 4	027	Jupiter	Test of short exposure times ($\leqslant$10 ms)
	2006 Sep 29	013	N/A	Solar scattered light (3-axis)
	2006 Sep 24	020	M7	Mosaic and geometric distortion
	2007 Jan 10	023	Callirrhoe	First test of RCM ($t_{\rm exp}$ = 5, 10 s)
ACO-1	2007 Sep 29	013	N/A	Solar scattered light (3-axis)
	2007 Oct 29	050	N/A	Functional test
ACO-2	2008 Oct 13	047	N/A	Solar scattered light (spinning)
	2008 Oct 15	043	N/A	Functional test
ACO-3	2009 Jul 21	050	N/A	Functional test
ACO-4	2010 Jun 24	047	N/A	Solar scattered light (spinning)
	2010 Jun 25	043	M7	Optical performance, Functional
ACO-5	2011 May 23	050	N/A	Functional test
ACO-6	2012 May 23	050	N/A	Functional test
	2012 Jun 1	055	M7	Optical performance
ACO-7	2013 Jun 22	050	N/A	Functional test
	2013 Jul 2	080	M7	Optical performance
	2013 Jul 3	081	NGC 3532	Optical performance
ACO-8	2014 Jul 5	050	N/A	Functional test
	2014 Jul 22	082	NGC 3532	Optical performance
Cal Campaign	2016 Jul 3	050	N/A	Functional test
	2016 Jul 11	081	NGC 3532	Optical performance
	2016 Jul 14	102	HD 37962	Absolute calibration
	2016 Jul 16	103	HD 205905	Absolute calibration
	2017 Sep 18	081a	NGC 3532	Verify performance after 100 days without decontamination
	2017 Dec 5	081 c	NGC 3532	Verify performance after 180 days without decontamination

Note. "ACO" stands for "Annual Check Out." "SAP" stands for "Science Activity Plan." "CR" stands for "Cosmic Ray." "RCM" stands for "Relative Control Mode." "Functional" tests include bias images (0 ms exposure times), lamp exposures, and autoexposure images. All listed dates are in UTC in the spacecraft frame.

to convert from the observed count rate in a pixel to a radiance value at LORRI's pivot wavelength:

$$I = S/t_{\rm exp}/\text{RPLUTO (diffuse target)} \tag{8}$$

where:

I is the diffuse target radiance ($\mathrm{erg\,cm^{-2}\,s^{-1}\ \AA^{-1}\,sr^{-1}}$) at $\lambda_{\rm pivot}$.
S is the measured signal in a pixel (DN).
$t_{\rm exp}$ is the exposure time (s).
RPLUTO is the LORRI diffuse photometry keyword for targets with Pluto-like SEDs.

Since the solar flux ($F_\odot$) at a heliocentric distance of 1 au at the LORRI pivot wavelength is 176 $\mathrm{erg\,cm^{-2}\,s^{-1}\ \AA^{-1}}$, the value for the radiance can be converted to I/F (where $\pi F = F_\odot$), which is a standard photometric quantity used in planetary science, using:

$$I/F = \pi I r^2/F_\odot \tag{9}$$

$$\rightarrow I/F = (S/t_{\rm exp}/\text{RPLUTO}) * \pi r^2/F_\odot \tag{10}$$

where "r" is the target's heliocentric distance in astronomical units.

For unresolved targets (e.g., planetary targets observed at large ranges), the absolutely calibrated flux (also called the irradiance) at the LORRI pivot wavelength can be determined using the point source photometry keywords. For a target with an SED similar to that of MU69, the observed count rate integrated over the LORRI PSF can be related to the flux (not to be confused with "F" in "I/F") at the LORRI pivot wavelength by:

$$F = S_{\rm total}/t_{\rm exp}/\text{PMU69 (point target)} \tag{11}$$

where:

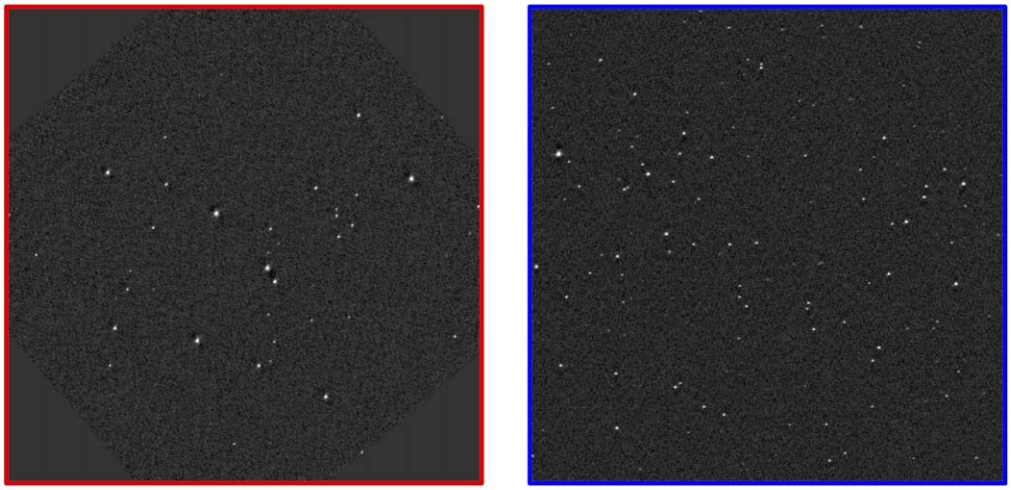

Figure 11. LORRI 1 × 1 images of M7 (left) and NGC 3532 (right) are displayed using the same hyperbolic sine (sinh) intensity stretch ranging from −0.2 to 100 DN. Both images are 100 ms exposures and are displayed with celestial north up and east left. Although M7 has brighter stars, NGC 3532 has a higher spatial density of stars, which provides better spatial coverage over the full LORRI field-of-view.
(A color version of this figure is available in the online journal.)

F is the point target flux, or irradiance (erg cm^{-2} s^{-1} Å^{-1}).
$S_{\rm total}$ is the total signal from the target integrated over the PSF (DN).
$t_{\rm exp}$ is the exposure time (s).
PMU69 is the LORRI point source photometry keyword for targets with MU69-like SEDs.

When observing stars, it is more common to convert the absolute flux to a magnitude in a standard photometric system. For an A-type star observed by LORRI, the V magnitude is given by:

$$V_{\rm star} = -2.5\log(S_{\rm total}/t_{\rm exp}) + {\rm ZPT} - 0.060 \qquad (12)$$

where $V_{\rm star}$ is the star's magnitude in the standard Johnson V band, $S_{\rm total}$ is the total signal integrated over the LORRI PSF (DN), $t_{\rm exp}$ is the exposure time (s), ZPT is the photometric zero-point (18.78 for 1 × 1 and 18.88 for 4 × 4), and the color correction term is −0.060.

3. In-flight Calibration Measurements and Results

In-flight LORRI calibration measurements started shortly after the launch of the *New Horizons* spacecraft on 2006 January 19 and have continued at regular intervals throughout the mission. The relevant calibration measurements conducted during the mission are listed in Table 4. The results from these observations are summarized in the following sub-sections.

3.1. Optical Performance

LORRI's optical performance has been monitored throughout the mission by observing star clusters. Measurements of the two-dimensional spatial distributions of individual stars enable characterization of the LORRI PSF across the entire FOV. Photometry of the individual stars is performed to monitor LORRI's sensitivity, both across the FOV and as a function of time. By using clusters whose stars are cataloged in one or more astrometric surveys, LORRI's geometrical distortion can also be measured and monitored as a function of time.

The galactic open cluster Messier 7 (M7; alternate names are NGC 6475 and the Ptolemy cluster) was used for LORRI's optical performance calibrations from 2006 through 2013. In 2013, we switched to the galactic open cluster NGC 3532 (alternate names are the Wishing Well cluster, the Pincushion cluster, and the Football cluster), primarily because NGC 3532 has a higher density of stars (Figure 11), which allows better areal coverage over the full CCD and improved mapping of LORRI's geometrical distortion. We observed *both* clusters during ACO-7 in 2013 so that later observations of NGC 3532 (i.e., those taken after 2013) could be compared to earlier observations of M7 (i.e., those taken between 2006 and 2013), thereby enabling systematic monitoring of LORRI's performance over the entire mission.

The optical design of LORRI has a small amount of pincushion distortion, which is clearly detected in measurements of the star clusters (Figure 12). However, LORRI achieved its design goal of keeping the geometrical distortion $\leqslant$0.3% over the entire FOV. Spot checks of the geometrical distortion at different times in the mission have not shown any significant differences (i.e., the various distortion parameters do not change by more than their measurement uncertainties, at the 2σ level). The LORRI geometrical distortion is described in detail in the SPICE instrument kernel for LORRI, which is archived at the Small Bodies Node (SBN) of the Planetary Data System

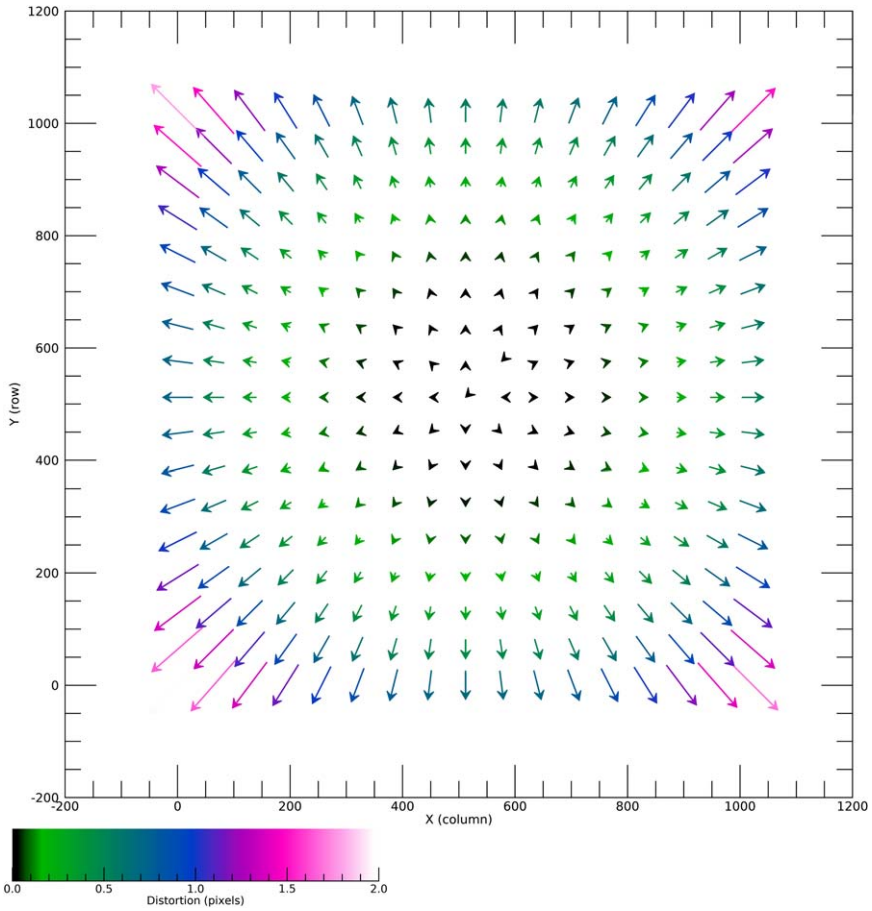

Figure 12. LORRI 1 × 1 geometrical distortion map derived from the analysis of an image of NGC 3532. At each plotted location on the CCD (i.e., CCD pixel coordinates), the arrow points in the direction of the distortion and its size is proportional to the magnitude of the distortion. The colors of the arrows encode the magnitude of the distortion in 1 × 1 pixels, as given in the colorbar. LORRI has a small amount of pin-cushion distortion, with the largest distortion occurring in the four corners, where the magnitude grows to 1.5 pixels.
(A color version of this figure is available in the online journal.)

(PDS). The geometrical distortion coefficients described within the Simple Image Polynomial (SIP) framework, which is commonly used in astronomy, are captured in the LORRI FITS header keywords. We note also that the archived LORRI FITS files employ World Coordinate System (WCS) keywords to enable accurate transformations between native LORRI [x, y] pixel locations and standard astronomical coordinates (e.g., [R.A., decl.]).

High S/N PSFs for both 1 × 1 and 4 × 4 LORRI images are displayed in Figure 13. These were created by combining multiple images of single stars located near the center of the LORRI FOV, including images taken with different exposure times to expand the dynamic range of the composite (e.g., for 1 × 1 images, using 100 ms exposures to sample the PSF cores and using 400 ms exposures to sample the PSF wings). Three diffraction spikes produced by the three struts of the OTA are clearly visible. The PSFs are not completely symmetrical; there is excess flux extending from the peak pixel toward the lower right, which is presumably produced by a slight misalignment of the OTA. This asymmetry in the PSF has been present at the same level throughout the mission, indicating it is a stable feature, which enables accurate deconvolution techniques to be applied when attempting to maximize the spatial resolution of LORRI images.

A technique for creating properly sampled (i.e., Nyquist sampled) PSFs is described in Lauer (1999) and has been applied to LORRI images when multiple, dithered exposures are available. A good example is the LORRI imaging of Pluto's satellite Kerberos, when four separate images could be combined to create a composite with significantly higher resolution than the individual images (Figure 14). Deconvolution can also be used to remove motion smear for LORRI images taken during scanning observations of the Ralph instrument (e.g., Figure 7).

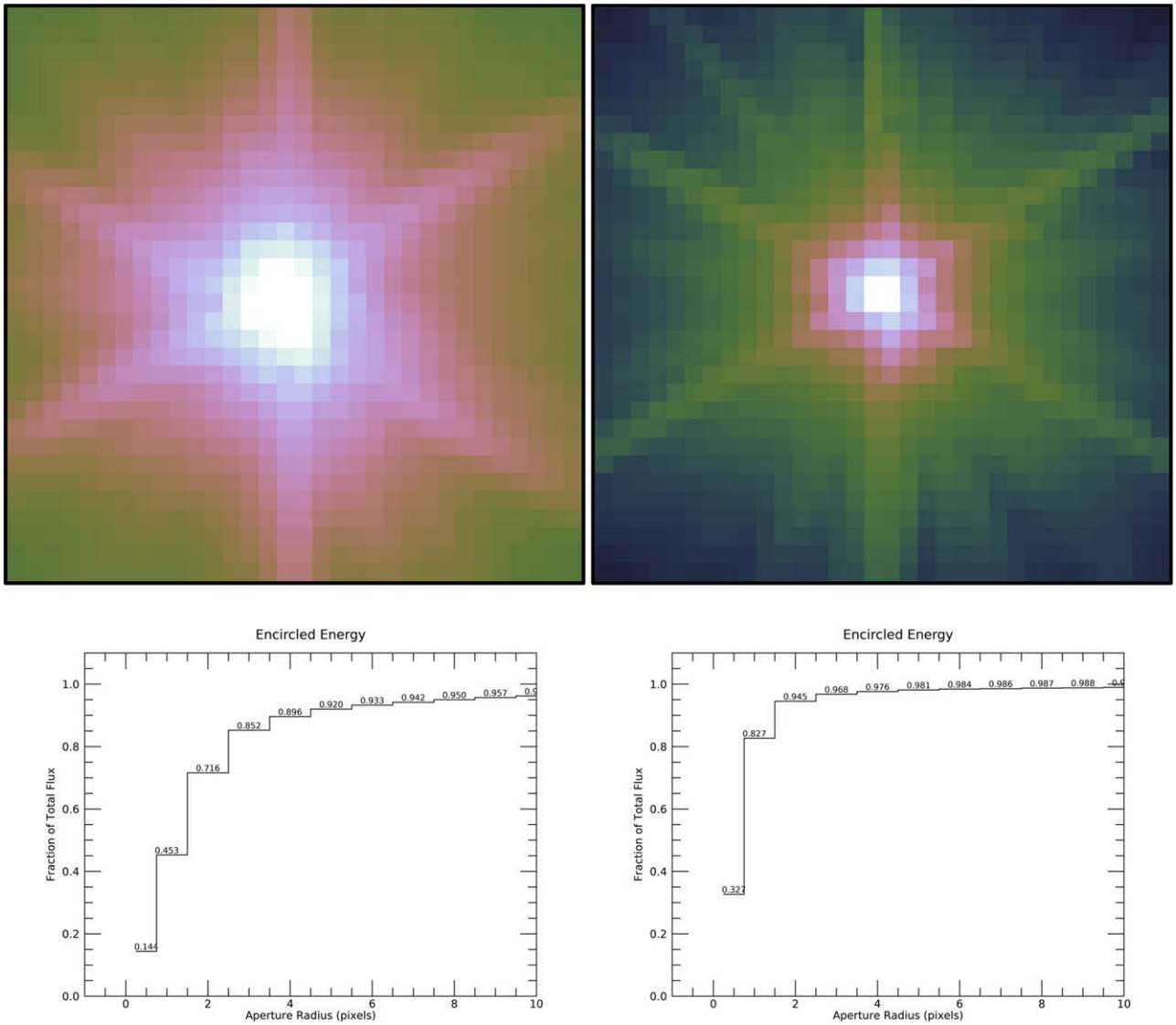

Figure 13. LORRI composite PSFs, valid for locations near the center of the CCD, are displayed for both 1 × 1 (upper left) and 4 × 4 (upper right) CCD formats. In both cases, 32 × 32 pixel regions are displayed using a hyperbolic sine (sinh) intensity stretch to show more clearly the full dynamic range of the image. Diffraction spikes from the three legs of the OTA spider are clearly evident. Encircled energy (EE) plots are displayed below each image; each data point is labeled with the fraction of light within the plotted radius. In 1 × 1 format, the peak pixel contains ∼14% of the total intensity. In 4 × 4 format, the peak pixel contains ∼32% of the total intensity.

(A color version of this figure is available in the online journal.)

Both the shapes and intensities of the stars in the calibration fields are used to determine whether there has been any degradation in the optical performance over the course of the mission. For example, contamination (e.g., ice accumulation) anywhere along LORRI's optical path could manifest as a reduction in photometric sensitivity and/or a broadening of the PSF. We monitor the PSF shape by fitting two-dimensional Gaussians to the stellar images each time the calibration fields are observed. We monitor LORRI's sensitivity by comparing the signals for the same stars measured at multiple epochs.

Figure 15 shows the results of the Gaussian fits to the stars measured during the observations of NGC 3532 during the calibration campaign in 2016 July. By comparing the PSFs from stars falling in five different regions of the CCD, we show how the PSF varies across the LORRI FOV. The PSF behavior exhibited in this figure is typical of what has been observed throughout the mission. Figure 16 explicitly compares the LORRI PSFs measured on M7 stars over a 5 yr period (2008–2013); there is no significant variation in the shape of the PSF over this period.

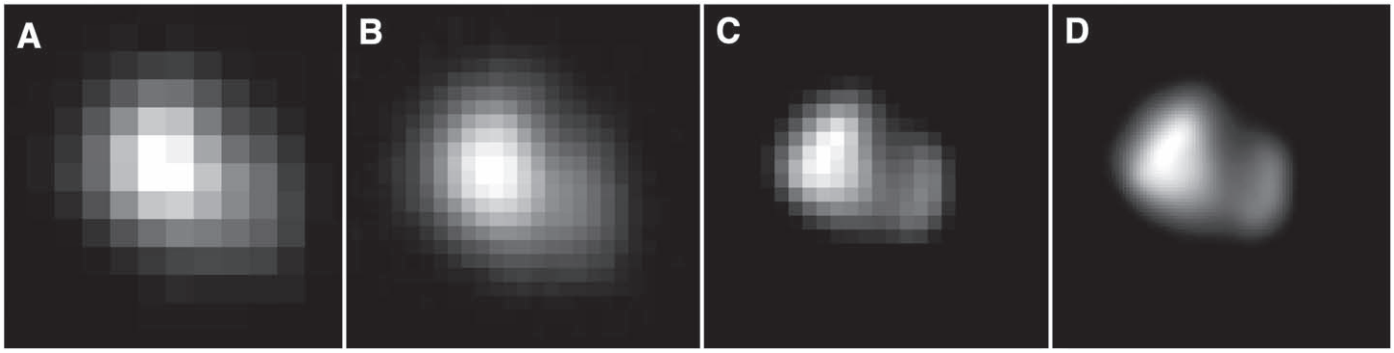

Figure 14. Demonstration of the image processing steps performed to produce a deconvolved LORRI image of Kerberos, one of Pluto's four small satellites. (A) A single calibrated LORRI image, one of four taken. (B) The interlaced and Nyquist-sampled "superimage" generated by combining the four calibrated images—the pixel scale is twice as fine as the native LORRI scale. (C) The superimage after applying Lucy–Richardson deconvolution. (D) The deconvolved image up-sampled by an additional factor of 4 for a final scale 8 times finer than the native LORRI scale. This latter step removes the pixelated appearance of the previous image for improved clarity, and is mathematically justified since the superimage is Nyquist-sampled. Adapted from Weaver et al. (2016).

The Gaussian fits applied to the star cluster images employed a ± 10 pixel region centered on each star's peak pixel, which includes both the core and a significant fraction of the wings of the spatial brightness distribution. Restricting the fit to the core only, which is a better measure of LORRI's spatial resolution, results in a narrower full width at half maximum (FWHM). For example, using the same Gaussian fitting routine on the 1×1 PSF displayed in Figure 13 gives (XFWHM, YFWHM) = (2.06, 2.65) pixels when a ± 10 pixel region is fit, and (XFWHM, YFWHM) = (1.87, 2.47) pixels when a ± 2 pixel region is fit. Thus, we see that the LORRI PSF is slightly undersampled (relative to Nyquist) in the X (row) direction.

Photometry of M7 stars over a 7 yr period (2006–2013) demonstrates that there has been no significant change in LORRI's sensitivity during this time (Figure 17). Photometry of NGC 3532 stars over a 4.5 yr period (2013 July–2017 December) also shows no significant change in LORRI's sensitivity during this period (Figure 18). Combining all these results, and taking into account that the stars being sampled did not necessarily have constant fluxes during the times of the LORRI measurements, we conclude that LORRI's sensitivity has remain essentially unchanged (at the level of $\sim$1%) over the entire duration of the mission.

3.2. Absolute Calibration

Since the SEDs of virtually all solar system targets are produced by scattered sunlight, we searched for absolute standard stars that are solar analogs to calibrate LORRI. Fortunately, two solar-type standard stars with absolute fluxes measured to an accuracy of $\sim$1% (1σ) by the *Hubble Space Telescope* (*HST*) have V magnitudes that are suitable for high S/N LORRI measurements, and they are also visible from the *New Horizons* spacecraft at reasonably large solar elongation angles for the entire mission.

HD 37962 has $V = 7.85$ and $B - V = 0.65$, which is identical to the solar color. This star was observed by LORRI on 2016 July 14, as part of the special post-Pluto calibration campaign. The solar elongation angle was 56°, and the solar scattered light level was negligible in all images. We obtained 5 different 100 ms exposures in 1×1 format and 5 different 50 ms exposures in 4×4 format. The observed stellar signals had S/N $\geqslant$ 140 in all 10 images. We used aperture photometry and the gain values discussed previously to calculate the total fluxes in electrons s^{-1}. As shown in Figure 19, the measured fluxes for the 1×1 and 4×4 images are in excellent agreement.

HD 205905 has $V = 6.74$ and $B - V = 0.62$, which is slightly bluer than solar color. This star was observed by LORRI on 2016 July 16, also as part of the special post-Pluto calibration campaign. We obtained 5 different 100 ms exposures in 1×1 format and 5 different 50 ms exposures in 4×4 format. The observed stellar signals had S/N $\geqslant$ 100 in all 10 images. The solar elongation angle was 144°, and the solar scattered light level was negligible in all images. The photometry results for HD 205905 are fully consistent with the results obtained from HD 37962.

Figure 20 shows a comparison of the stellar and solar spectra. Given the remarkably solar-like SED for HD 37962, we decided to use that star as the primary LORRI absolute calibration standard. Assuming that LORRI's relative responsivity (see the next section) as a function of wavelength was accurately measured during the ground calibration (Morgan et al. 2005), we adjusted the absolute scale of the responsivity curve using a single constant multiplicative factor to force the *calculated* signal from HD 37962 to match the *observed* signal. The calculated signal is the integral over all wavelengths of the product of the star's SED in absolute units and LORRI's responsivity curve. The new LORRI responsivity curve produced in this way is discussed in the next section.

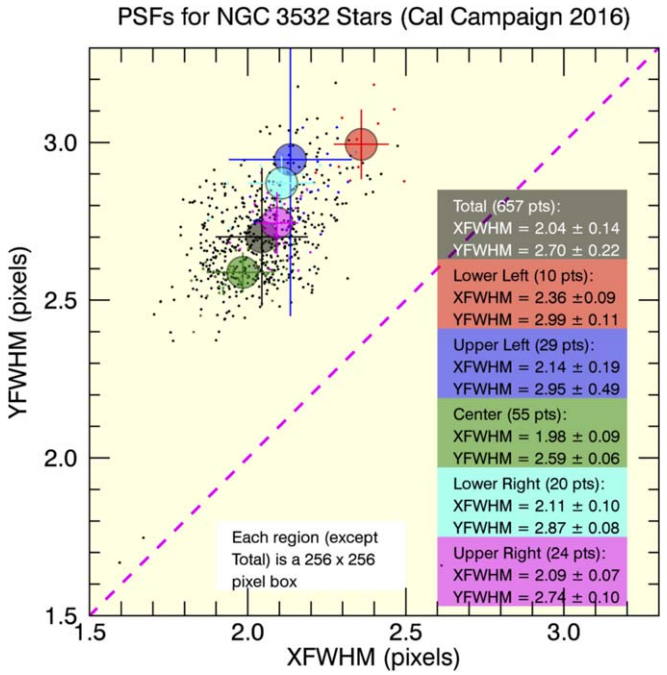

Figure 15. Two-dimensional Gaussian fits to the spatial brightness distributions of stars in NGC 3532 observed during the calibration campaign in 2016 July are plotted. The LORRI boresight was moved around in a 3 × 3 raster pattern centered on the nominal position of NGC 3532, which enabled 657 separate measurements of the point-spread function (PSF) across the CCD. The $+x$-dimension corresponds to the direction of increasing CCD columns, and the $+y$-dimension corresponds to the direction of increasing CCD rows. Subgroups of the stars have been color coded as a function of their locations on the CCD. Each sub-group is comprised of stars located in a 256 × 256 pixel region on the CCD, as indicated in the figure. The CCD has an optically active region of 1024 × 1024 pixels. The average full width half maximum (FWHM) in each dimension, the standard deviation of the FWHMs, and the number of stars in each sub-group, are listed and plotted for each location. The FWHMs and their standard deviations for all the stars, independent of location, are also listed and plotted. The points would lie along the dashed diagonal line if the PSFs had the same widths in the two directions, but YFWHM is systematically larger than XFWHM due to the shape of the asymmetric PSF and the better charge transfer efficiency in the x-direction. See the text for further discussion.
(A color version of this figure is available in the online journal.)

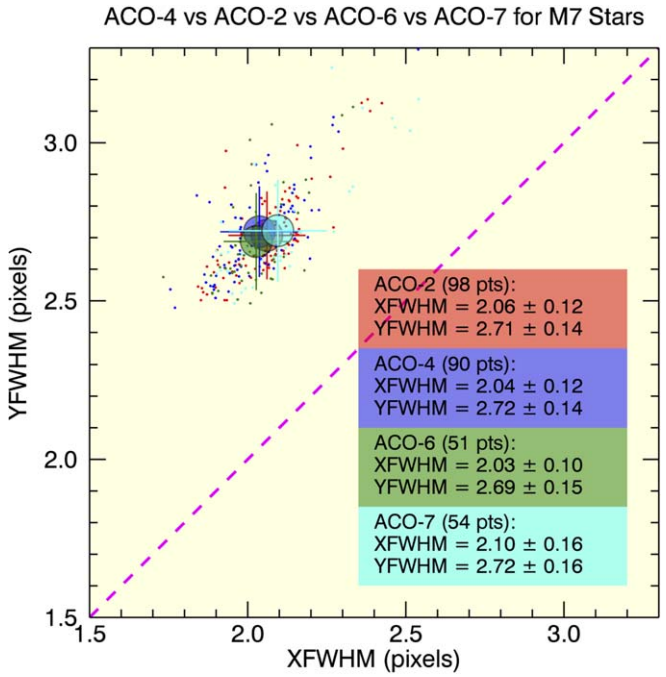

Figure 16. Two-dimensional Gaussian fits to the spatial brightness distributions of multiple stars in the open galactic cluster M7 are plotted for four different epochs. The $+x$-dimension corresponds to the direction of increasing CCD columns, and the $+y$-dimension corresponds to the direction of increasing CCD rows. The average full width half maximum (FWHM) in each dimension, and the standard deviation of the FWHM, are listed and plotted for each epoch. ACO is an acronym for "Annual Check Out." See the text for further discussion.
(A color version of this figure is available in the online journal.)

For targets having solar-type SEDs, the absolute accuracy of the values derived from LORRI data should be comparable to the accuracy of the *HST* measurements (i.e., ∼1%, 1σ) because the LORRI calibration is tied to the absolute flux from HD 37962. However, the accuracy of the LORRI calibration also depends on the accuracy with which the total measured LORRI signal from HD 37962 is determined. The peak pixel during these measurements has S/N $\geqslant$ 100, but we use aperture photometry with a radius of 5 pixels (for 1 × 1 images; we used a 3 pixel radius aperture for 4 × 4 images) to measure the signal and then use the PSF described in Section 3.1 to correct to the signal for an infinite aperture (i.e., integrated over the PSF). The absolute accuracy of this latter estimation process is probably a few percent. We note that the *relative* photometry of different solar-type stars is set by the S/N of the individual measurements, which can be considerably more accurate than the absolute flux measurement.

For targets with SEDs significantly different than solar-type, the LORRI calibration is dependent on the accuracy of the *shape* of LORRI's responsivity curve, as determined from the ground calibration (Morgan et al. 2005). As discussed there, we assumed that the wavelength dependence of the responsivity followed the prescriptions provided by the various vendors contributing to the LORRI hardware. While these prescriptions usually involved measurements made on actual LORRI hardware (e.g., transmittance measurements for the optical components), we assumed a QE curve for the CCD that followed the "typical" response specified by the manufacturer for the anti-reflection layer ordered for the LORRI CCD. The shape of the CCD QE curve is thought to be accurate to a few percent in the regions of high QE (i.e., for most of the wavelength range covered by LORRI), but larger variations in QE are possible in the steeply sloped portions of the QE curve.

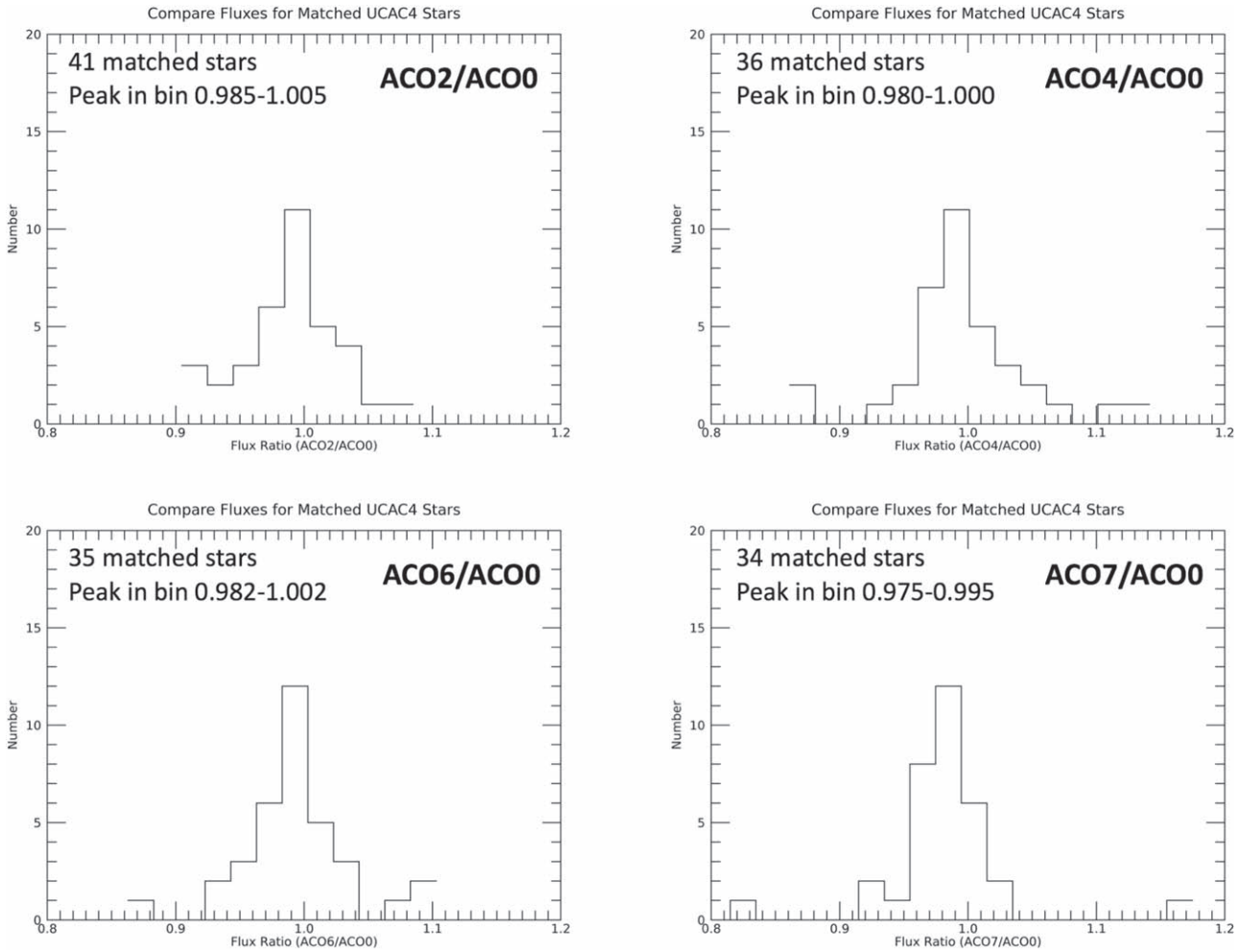

Figure 17. LORRI aperture photometry of stars in M7 at four different epochs is compared to that measured on 2006 August 31 (ACO-0), immediately after the telescope door was opened. For each epoch, a histogram is plotted showing the ratio of the observed stellar fluxes to the fluxes measured for those same stars in 2006. The number of matched stars is displayed on each plot. The histogram bin widths are 0.02, and the bin location of the peak in the distribution is listed on each plot. ACO is an acronym for "Annual Check Out." See the text for further discussion.

Given the wide bandpass of LORRI, these latter variations will likely not significantly affect the measured signals from LORRI's targets. For all these reasons, we suggest that the absolute accuracy for LORRI observations of non-solar-type targets is probably ~10%, and possibly significantly better than that, approaching the accuracy achieved for targets with solar-type SEDs.

3.3. Responsivity Curves

For a photon counting optical system like LORRI, the signal detected (S_e in electrons) in an image pixel with exposure time $t_{\rm exp}$ (in seconds) can be expressed as:

$$S_e = t_{\rm exp} * A * \Omega * \int_\lambda I * {\rm QE}\, d\lambda \quad \text{(diffuse target)} \qquad (13)$$

and:

$$S_e = t_{\rm exp} * A * {\rm EE} * \int_\lambda F * {\rm QE}\, d\lambda \quad \text{(point target)} \qquad (14)$$

where:

A is the unobscured aperture area of the OTA (339.8 $\rm cm^2$).
Ω is the IFOV (2.464×10^{-11} sr for 1×1, 3.942×10^{-10} sr for 4×4).
I is the diffuse target radiance (photons $\rm cm^{-2}\, s^{-1}\, \AA^{-1}\, sr^{-1}$).
F is the point target flux (photons $\rm cm^{-2}\, s.^{-1}\, \AA^{-1}$).
EE is the fraction of the point source flux captured in the peak pixel.
QE is the total system quantum efficiency.

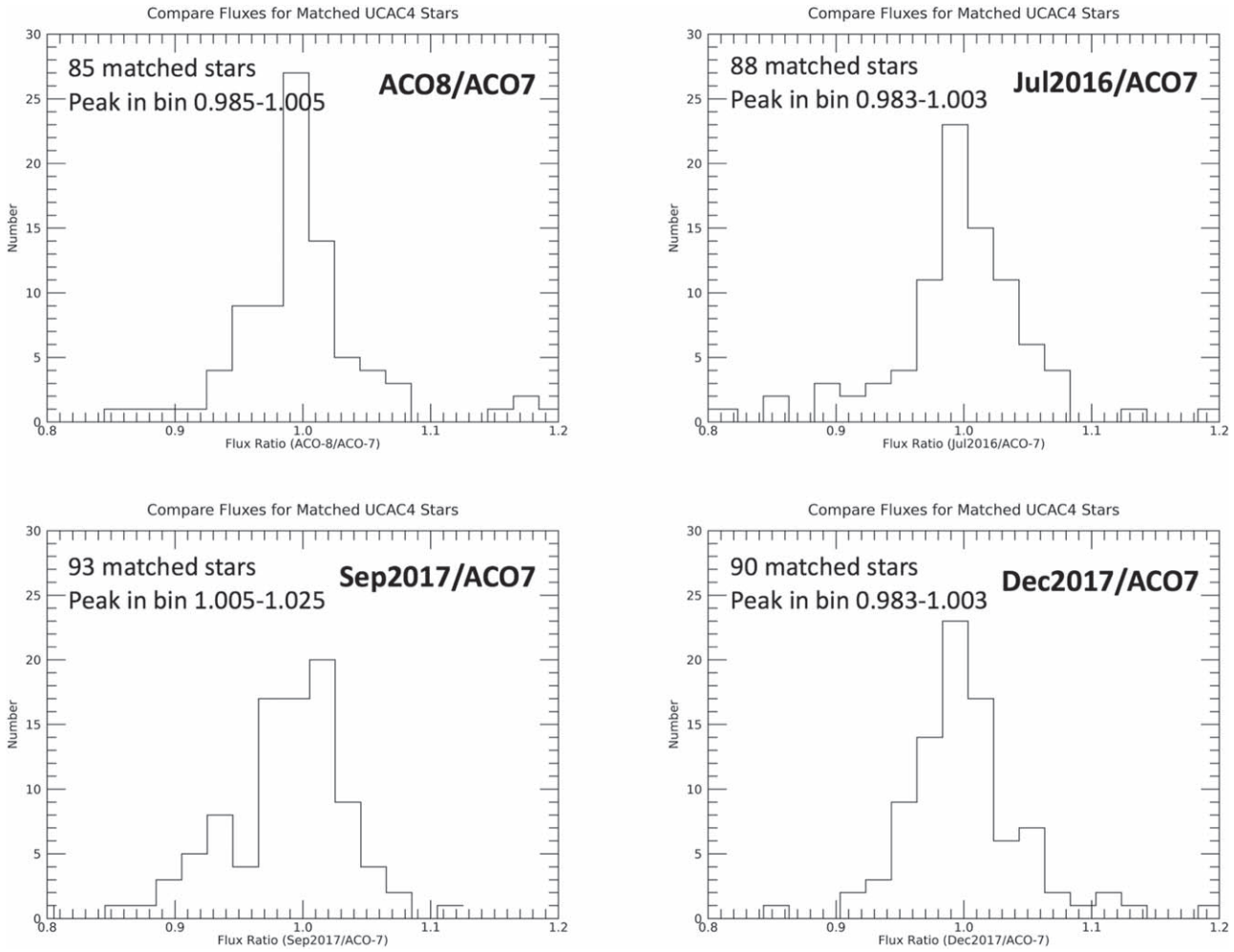

Figure 18. LORRI aperture photometry of stars in NGC 3532 at four different epochs is compared to that measured on 2013 July 3 (ACO-7). For each epoch, a histogram is plotted showing the ratio of the observed stellar fluxes to the fluxes measured for those same stars in 2013. The number of matched stars is displayed on each plot. The histogram bin widths are 0.02, and the bin location of the peak in the distribution is listed on each plot. ACO is an acronym for "Annual Check Out." See the text for further discussion.

The noise (N in electrons) in a LORRI image pixel can be expressed as (for both diffuse and point targets):

$$N = \sqrt{S_e + \mathrm{SL} + \mathrm{FT} + (I_\mathrm{d} * t_\mathrm{exp}) + \mathrm{RN}^2} \qquad (15)$$

where:

SL is the signal produced by solar scattered light (e).
FT is the signal produced by the CCD frame scrub and transfer process (i.e., smear) (e).
I_d is the CCD dark current ($e\,\mathrm{s}^{-1}$ pixel^{-1}).
RN is the electronics noise (e, including the CCD read noise).

The LORRI solar scattered light level (SL) has been measured multiple times during the mission (Table 4). For solar elongation angles (SEAs) smaller than ~30°, the scattered light level varies as a function of the spacecraft roll angle. Figure 21 shows a model for the I/F of the solar scattered light level as a function of SEA. The model falls roughly halfway between the smallest and largest observed scattered light values. At small SEAs, the actual I/F of the solar scattered light could be up to a factor of two times smaller or larger than the model value. The model I/F values are independent of the spacecraft's heliocentric distance (r), but the CCD signal rate (DN s^{-1}) has an r^{-2} dependence. The SEA at which the solar scattered light produces a signal rate of 10 DN s^{-1} pixel^{-1} (i.e., ~10× larger than the electronics noise) is shown in the figure for the heliocentric distances of the *New Horizons* flybys (i.e., at Jupiter, Pluto, and MU69).

The LORRI team created an exposure time calculator (ETC) that uses the above formalism to estimate S/Ns for planned

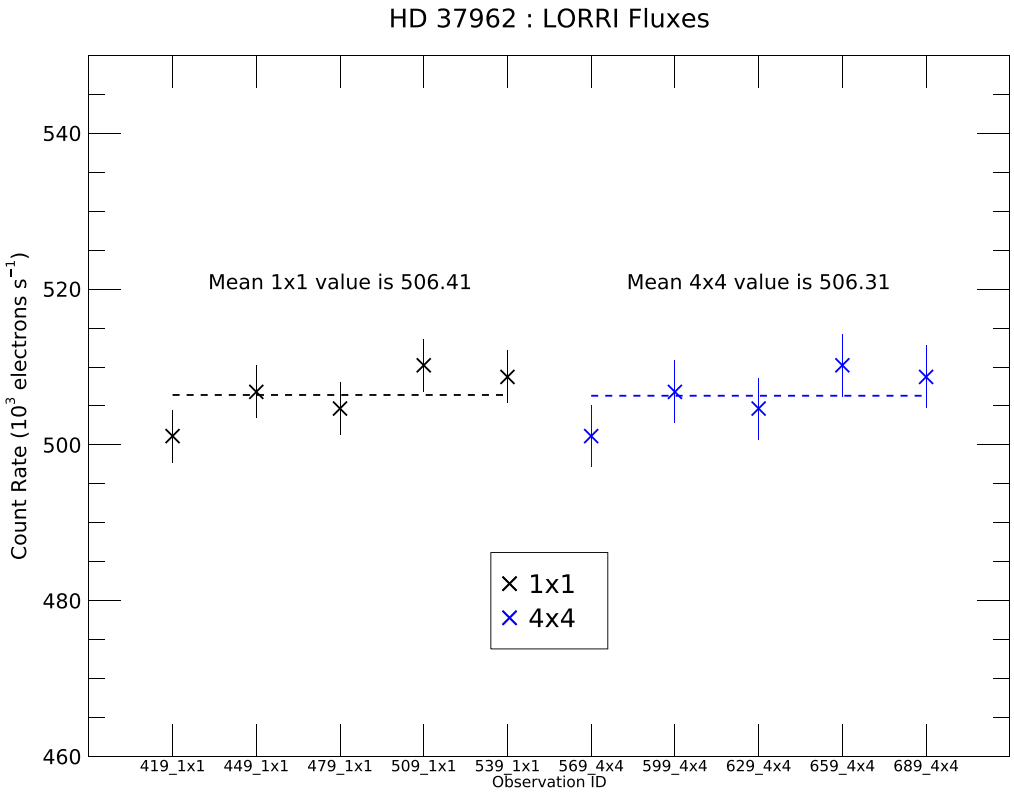

Figure 19. The total fluxes from the absolute calibration standard star HD 37962 are plotted for five different 1 × 1 images and for five different 4 × 4 images. For the 1 × 1 images, the stellar fluxes were derived by integrating the signal in a 5 pixel radius aperture centered on the star and then subtracting a background level (almost negligible) derived from the average signal in an annulus extending between 10 and 20 pixels from the star. For the 4 × 4 images, the stellar fluxes were derived by integrating the signal over a 3 pixel radius aperture centered on the star and then subtracting a background level (almost negligible) derived from the average signal in an annulus extending between 10 and 20 pixels from the star. These aperture fluxes were then corrected to total fluxes (i.e., integrated over the entire PSF) using the encircled energy curves presented in Figure 13. The "Observation ID" is a concatenation of the 3 least significant figures in the mission elapsed time (MET) for each observation and the CCD format used. The first image in each sequence shows a slightly lower flux than measured in subsequent images, for both 1 × 1 and 4 × 4 formats, possibly suggesting a "start-up" effect. However, the effect is small ($\lesssim$1%) and appears to resolve within ∼30 s, which is the spacing between consecutive images for these observations.
(A color version of this figure is available in the online journal.)

observations. The ETC can also be used estimate target signals in absolute units by comparing observed S/Ns to S/Ns reported by the ETC. For point sources with S/N $\geqslant$ 5 in a single pixel, the S/N can typically be improved by a factor of ∼2 by summing the signal over several pixels (aperture photometry) or by employing PSF-fitting photometry.

The LORRI signal level depends on two key parameters: the total system quantum efficiency (QE) and (in the point source case) the amount of energy from a point source concentrated in a single pixel (EE). LORRI's EE was discussed in the previous subsection, so we focus on QE here.

For LORRI, the QE is given by:

$$\mathrm{QE} = L_{\mathrm{obscure}} * T_{\mathrm{optics}} * \mathrm{QE}_{\mathrm{CCD}} \quad (16)$$

where:

L_{obscure} is the loss factor associated with obscuration by the secondary mirror and OTA spider.

T_{optics} is the total transmittance of all optical elements.

$\mathrm{QE}_{\mathrm{CCD}}$ is the quantum efficiency of the CCD.

Although not explicitly stated, all quantities in the equation above are a function of wavelength. Prior to any system calibration measurements, LORRI's QE was estimated from Equation (16) using component level measurements from manufacturers. The original LORRI ETC also relied on these component level measurements. The system level QE was determined from ground calibration measurements (Morgan et al. 2005), and those measurements were used to update the ETC. Subsequently, in-flight measurements of absolute calibration standard reference stars (see the previous section) were used to further refine LORRI's absolute responsivity. The final LORRI absolute calibration is essentially a hybrid product, with the wavelength dependence determined from the ground calibration (when filters could be used to restrict the wavelengths sampled) and with the absolute sensitivity

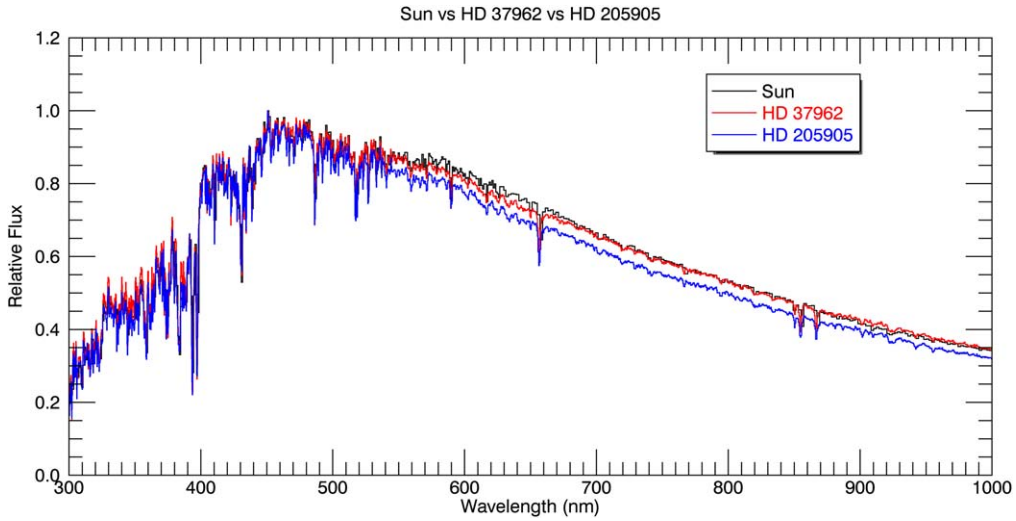

Figure 20. The spectral energy distribution (SED) of the two absolute calibration standard stars used by LORRI (HD 37962 and HD 205905) are compared to the solar spectrum. All spectra are normalized to their peak values. The SED of HD 37962 is particularly close to that of the Sun, so this star was selected as the primary standard star for LORRI absolute sensitivity calibrations.
(A color version of this figure is available in the online journal.)

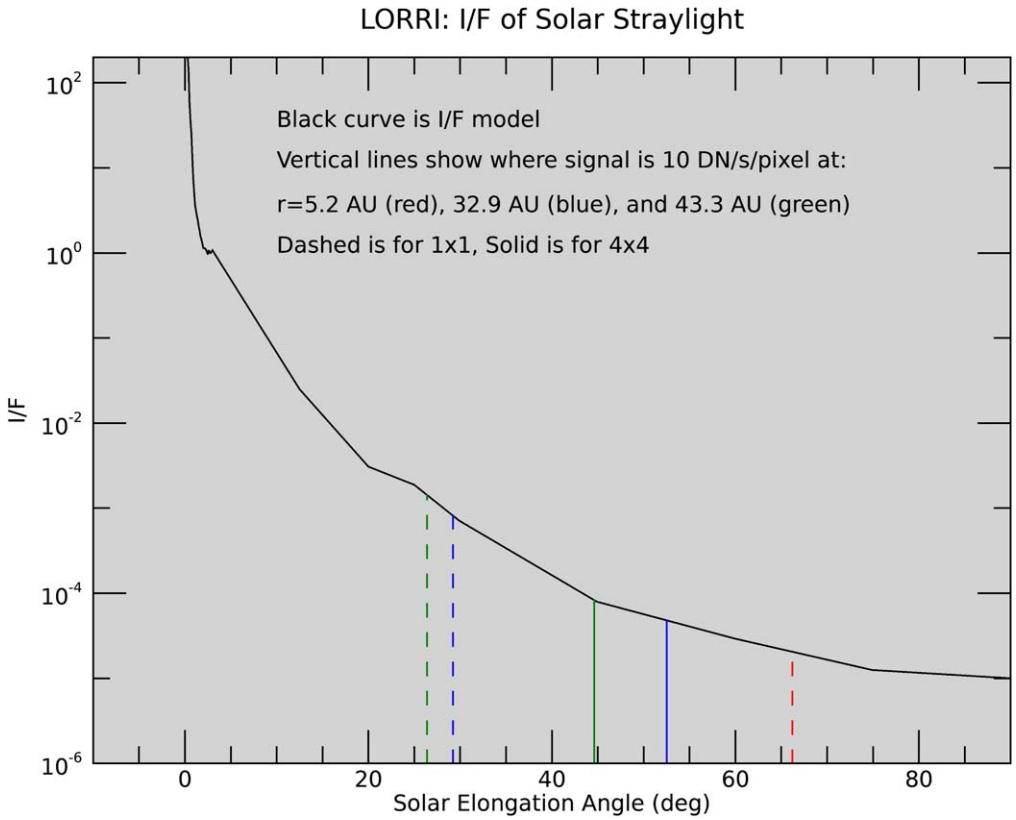

Figure 21. A model for the LORRI scattered light level is plotted as a function of solar elongation angle (SEA). The SEA at which the solar scattered light produces a signal rate of 10 DN s^{-1} $pixel^{-1}$ (i.e., $\sim$10$\times$ larger than the electronics noise) is shown in the figure for the heliocentric distances of the *New Horizons* flybys (i.e., at Jupiter, Pluto, and MU69).
(A color version of this figure is available in the online journal.)

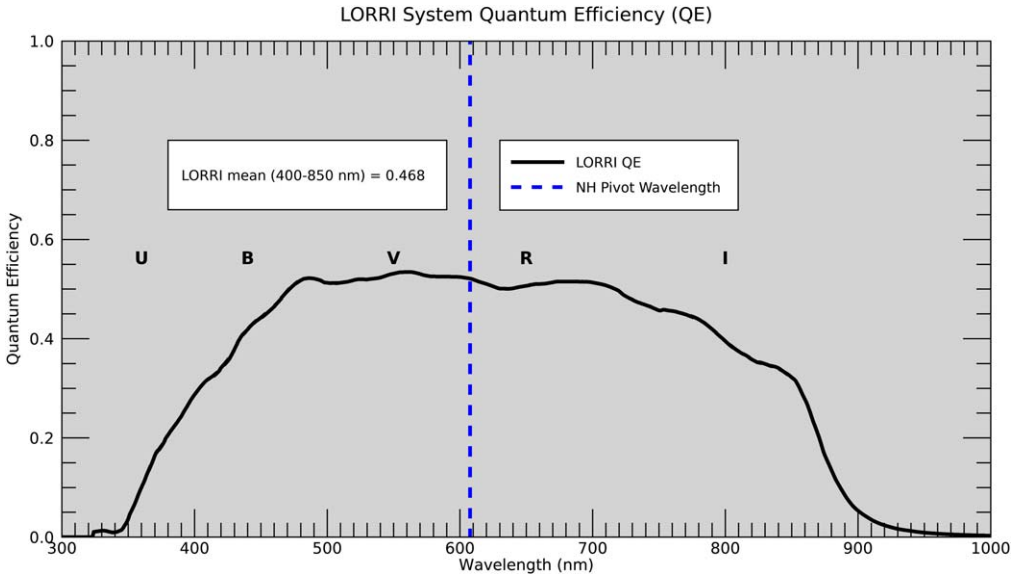

Figure 22. LORRI's system quantum efficiency (QE) is plotted as a function of wavelength. The mean QE over the wavelength range 400–850 nm is ∼47%. The locations of the LORRI pivot wavelength and the standard visible photometric bands (in the Johnson–Landolt system) are also shown. LORRI's pivot wavelength is located between the standard *V* and *R* band wavelengths.
(A color version of this figure is available in the online journal.)

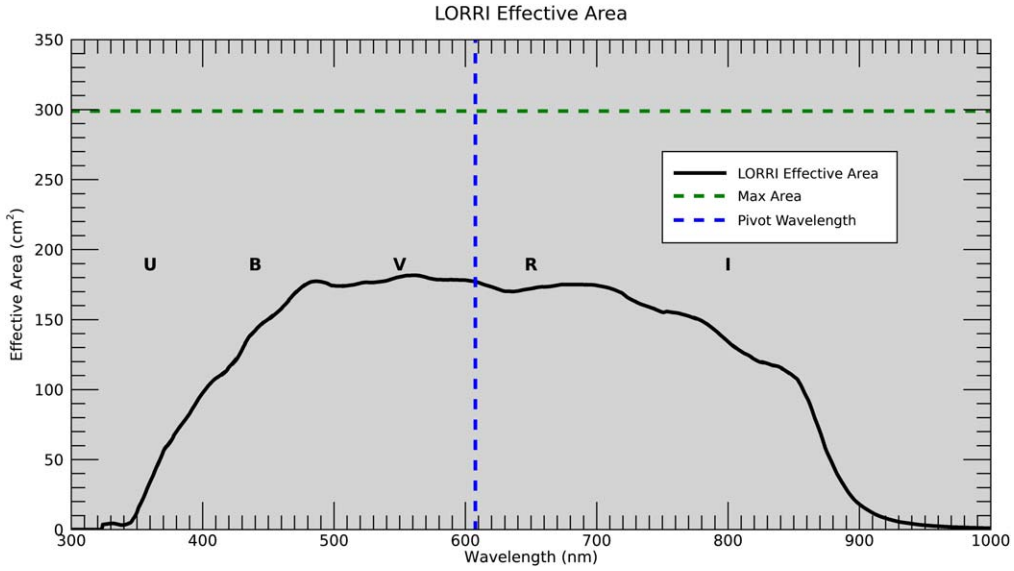

Figure 23. LORRI's effective area is plotted as a function of wavelength. Given the estimated LORRI obscuration of ∼11%, the theoretical maximum effective area is given by the green dashed line. The locations of the LORRI pivot wavelength and the standard visible photometric bands are also shown.
(A color version of this figure is available in the online journal.)

determined by scaling the wavelength-dependent curve by whatever factor is needed to force a match between the predicted and observed LORRI signals for observations of the absolute calibration standard stars.

Figure 22 shows the LORRI system QE as a function of wavelength, as determined from the absolute calibration measurements of the solar-type reference star HD 37962. The LORRI system QE is approximately 50% over much of the visible wavelength range (e.g., 480–700 nm). LORRI is a panchromatic instrument, which means that its output signal is proportional to the integral over all wavelengths of the product of the QE and the target's SED.

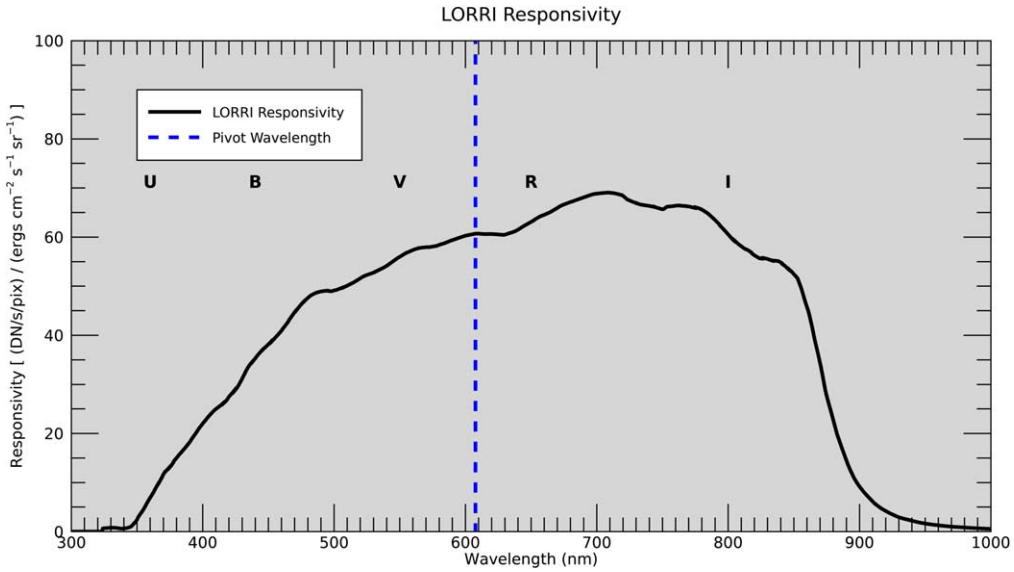

Figure 24. LORRI's absolute responsivity is plotted as a function of wavelength. The locations of the LORRI pivot wavelength and the standard visible photometric bands are also shown.
(A color version of this figure is available in the online journal.)

Note that the commonly used quantity "effective area" ($A_{\rm eff}$) of the optical system is just the area of LORRI's input aperture ($A = \pi * 20.8^2/4 = 339.8$ cm^2) multiplied by the system QE. Given the estimated LORRI obscuration of ~11% (i.e., $L_{\rm obscure} = 0.89$), the largest possible effective area for LORRI is ~300 cm^2. Figure 23 shows the LORRI effective area as a function of wavelength.

The LORRI absolute responsivity curve, which is used to calculate the photometry keywords, can be derived from the QE curve using the following equation:

$$R_\lambda = A_{\rm eff} * \Omega * \lambda/{\rm gain}/hc \quad (17)$$

where:

R_λ is the responsivity ((DN s^{-1} pixel^{-1})/(erg cm^{-2} s^{-1} sr^{-1})).
$A_{\rm eff}$ is the effective area as defined above (cm^2).
Ω is the solid angle of a single pixel (sr).
λ is the wavelength of interest (nm).
gain is the CCD gain (21 e DN^{-1} for 1 × 1 format).
hc is the product of Planck's constant and the speed of light (1.986×10^{-16} J nm).

Figure 24 shows the LORRI responsivity curve as a function of wavelength for 1 × 1 format, as derived from the measurements of the absolute calibration standard star HD37962. The responsivity curve for 4 × 4 format can be obtained by multiplying the 1 × 1 curve by the constant 17.1.

4. Summary

LORRI's key design parameters are summarized in Table 5. LORRI has played a major role in the success of the *New Horizons* mission by serving as the primary optical navigation camera, by providing the highest resolution measurements of the mission's flyby targets, and by performing high sensitivity observations of remote targets at unique geometries.

Assuming that the wavelength variation of LORRI's sensitivity is accurately described by the ground-based calibration, LORRI's absolute sensitivity should be accurate to ~2% (1σ) for targets with solar-type SEDs. The accuracy of the absolute calibration for targets with other SEDs should be comparably good when employing synthetic photometry techniques, which we do when deriving LORRI's photometry keywords.

LORRI's sensitivity and optical performance are essentially unchanged since the launch of the *New Horizons* mission in 2006 January, more than 13 yr ago. Although LORRI is a "single string" instrument, susceptible to a single point failure to one of its critical components, its longevity is testimony to its simple, yet powerful, design. Indeed, the next generation of LORRI is currently being built to serve similar functions on NASA's *Lucy* mission, which is scheduled to launch in 2021 October when it will begin a program to perform the first flyby measurements of six Jovian Trojans (Levison et al. 2017).

We thank the scientists, engineers, and managers at APL who participated in the design, construction, and

Table 5
Summary of LORRI Key Parameters

Item	Description
Optical Telescope Assembly (OTA)	L3H-SSG Ritchey–Chrétien optical design with 3-element field flattener lens assembly
	Silicon Carbide (SiC) structure, SiC mirrors coated with high reflectance dielectric
	20.8 cm primary mirror diameter, ∼11% central obscuration
	Focal length = 261.908 cm
	Plate scale = 0.381813 μrad μm^{-1} = 787.″546 mm^{-1}
	NH OTA in-flight operating temperature is approximately −70 °C
	No moving parts, except for once-open telescope cover mounted to spacecraft
Focal Plane Characteristics	Teledyne-e2v 47–20 frame transfer CCD detector
	CCD frame transfer time ≈12 ms
	1024 × 1024 optically active pixels, 13 μm square pixels
	AR-coated, backside-thinned, backside-illuminated CCD
	1 × 1 and 4 × 4 (rebinned) output formats
	IFOV (1 × 1format) = 4.9636 μrad = 1.″0231 (square)
	FOV = 5.0827 milliradians = 0.°29122 (square)
	CDS with 12 bit ADC
	Full well ≈80,000 *e* (linear range)
	Anti-blooming technology to mitigate the effects of saturated targets in the FOV
	Electronics noise ≈24 *e*
	Dynamic range ≈3500 (single image)
	Gain: 21.0 *e* DN^{-1} (1 × 1), 19.4 *e* DN^{-1} (4 × 4)
	Dark current ⩽0.040 *e* s^{-1} pixel^{-1} (1 × 1at *NH* operating temperature of −81 °C)
	Available exposure times: 0–64,967 ms at 1 ms spacings
	1 Hz maximum frame rate (minimum time between consecutive images is 1 s)
Wavelength Range	Panchromatic (no filters) with ∼50% peak QE
	435–870 nm at 50% of peak QE
	360–910 nm at 10% of peak QE
Photometric Accuracy	∼2% (1σ) absolute for solar-type SED
	⩽10% (1σ) absolute for non-solar-type SEDs
	⩽1% (1σ) relative for S/N ⩾100
	Stable sensitivity at ∼1% level for ⩾13 yr

Note. "*NH*" stands for "*New Horizons*," "CCD" stands for "charge coupled device," "IFOV" stands for "individual pixel field of view," "FOV" stands for "field of view," and "AR" stands for "anti-reflection." "CDS" refers to "correlated double sampling," "ADC" refers to analog-to-digital converter, "QE" stands for "quantum efficiency," "SED" stands for "spectral energy distribution," and "S/N" stands for "signal-to-noise ratio."

testing of LORRI prior to launch: J. Boldt, K. Cooper, H. Darlington, M. Grey, J. Hayes, P. Hogue, T. Magee, E. Rossano, and C. Schlemm. We thank G. Rogers for his outstanding and innovative support of the spacecraft pointing operations, which enabled the LORRI observing program. We thank the *New Horizons* system engineering team (D. Kusnierkiewicz, C. Hersman, V. Mallder, G. Rogers) for its excellent work in maintaining the health and safety of the spacecraft. We thank S. Williams and A. Mick for their outstanding support of the *New Horizons* command and data handling system, including their management of complex solid state recorder operations. We thank the *New Horizons* Mission Operations team (especially A. Bowman, K. Whittenburg, and H. Hart) for its expert implementation of the LORRI observational program. We thank the *New Horizons* Science Operations team (E. Birath, A. Harch, D. Rose, and N. Martin) for its expert scheduling of the LORRI observations and data downlink. We thank M. Holdridge for his leadership during the Pluto and MU69 flyby campaigns. We thank the personnel at NASA's Deep Space Network for their support of communications with the *New Horizons* spacecraft, including the downlinking of the mission engineering and science data. We thank the *New Horizons* Project Managers, G. Fountain and H. Winters, for their steadfast support of LORRI throughout the mission. We thank B. Carcich for developing a computational shortcut for the original desmear calculations. We thank R. Bohlin for discussions regarding absolute calibration standards. We thank the personnel at SSG Precision Optronics (now L3-Harris SSG) who played major roles in building the LORRI OTA: F. Azad, K. E. Kosakowski, and D. Sampath.

Software: Interactive Data Language (IDL), licensed by the Harris Corporation.

ORCID iDs

H. A. Weaver https://orcid.org/0000-0003-0951-7762
A. F. Cheng https://orcid.org/0000-0001-5375-4250
T. R. Lauer https://orcid.org/0000-0003-4015-2730
W. M. Owen https://orcid.org/0000-0001-6096-4838

References

Cheng, A. F., Conard, S. J., Weaver, H. A., Morgan, F., & Noble, M. 2010, Proc. SPIE, 7731, 77311A
Cheng, A. F., Weaver, H. A., Conard, S. J., et al. 2008, SSRv, 140, 189
Conard, S. J., Azad, F., Boldt, J. D., et al. 2005, Proc. SPIE, 5906, 407
Conard, S. J., Weaver, H. A., Núñez, J. I., et al. 2017, Proc. SPIE, 10401, 104010W
Janesick, J. R. 2001, Scientific Charge-coupled Devices (Bellingham, WA: SPIE Optical Engineering Press)
Lauer, T. R. 1999, PASP, 111, 227
Levison, H. F., Olkin, C., Noll, K. S., Marchi, S. & Lucy Team 2017, in 48th Lunar and Planetary Science Conf. (The Woodlands, TX), 2025
McMichael, R. T., & Bentley, J. 2012, Proc. SPIE, 8486, 848602
Moore, J. M., McKinnon, W. B., Spencer, J. R., et al. 2016, Sci, 351, 1284
Morgan, F., Conard, S. J., Weaver, H. A., et al. 2005, Proc. SPIE, 5906 421
Noble, M. W., Conard, S. J., Weaver, H. A., Hayes, J. R., & Cheng, A. F. 2009, Proc. SPIE, 7441, 74410Y
Owen, W. M., Weaver, H. A., & Cheng, A. F. 2019, PASP, 132, 014504
Weaver, H. A., Buie, M. W., Buratti, B. J., et al. 2016, Sci, 351, aae0030
Weaver, H. A., Gibson, W. C., Tapley, M. B., Young, L. A., & Stern, S. A. 2008, SSRv, 140, 75
Zemcov, M., Arcavi, I., Arendt, R., et al. 2018, PASP, 130, 115001
Zemcov, M., Immel, P., Nguyen, C., et al. 2017, NatCo, 8, 15003